Research Paper

GEOSPHERE

GEOSPHERE, v. 19, no. 5

https://doi.org/10.1130/GES02617.1

14 figures; 4 tables

CORRESPONDENCE: xijunliu@glut.edu.cn

CITATION: Huang, W.-M., Liu, X.-J., Liu, L., Li, Z.-L., Liu, X., and Wu, H., 2023, Early Triassic roll-back of subducted Paleo-Tethys oceanic lithosphere: Insights from A_2-type silicic igneous rocks in the Pingxiang area, southwest China: Geosphere, v. 19, no. 5, p. 1372–1398, https://doi.org/10.1130/GES02617.1.

Science Editor: Christopher J. Spencer

Received 21 October 2022
Revision received 18 April 2023
Accepted 27 May 2023

Published online 27 July 2023

Early Triassic roll-back of subducted Paleo-Tethys oceanic lithosphere: Insights from A_2-type silicic igneous rocks in the Pingxiang area, southwest China

Wen-Min Huang[1], Xi-Jun Liu[1,2,*], Lei Liu[1,2,*], Zheng-Lin Li[1], Xiao Liu[1], and Hao Wu[1]

[1]Guangxi Key Laboratory of Hidden Metallic Ore Deposits Exploration, College of Earth Sciences, Guilin University of Technology, Guilin 541004, China
[2]Collaborative Innovation Center for Exploration of Nonferrous Metal Deposits and Efficient Utilization of Resource Guilin University of Technology, Guilin 541004, China

ABSTRACT

A suite of subduction-related early Triassic igneous rocks crops out in the Pingxiang area of the Dian-Qiong suture (DQS) in southwest China; this suite represents an important geological record of subduction and closure of the Paleo-Tethys Ocean. In this study, we report geochronological, geochemical, and Nd-Hf isotope data for newly discovered rhyolites and biotite granites in the Pingxiang area. We use these data to constrain their emplacement ages, origins, and geodynamic implications. Zircon U-Pb dating indicates that the rhyolites and biotite granites were emplaced at 251–250 Ma and 249 Ma (early Triassic), respectively. The rhyolites and biotite granites have elevated $FeO^T/(FeO^T + MgO)$ (0.78–0.89) and 10,000 × Ga/Al (2.83–4.11) ratios, with geochemical affinities to A_2-type granites. These rocks are enriched in some large-ion lithophile elements (e.g., Rb, Th, and Ba) and depleted in high-field-strength elements (e.g., Nb, Ta, and Ti), indicating their formation in a subduction-related arc. The rhyolites and biotite granites have negative whole-rock $\varepsilon_{Nd}(t)$ (–11.5 to –9.7) and zircon $\varepsilon_{Hf}(t)$ (–14.5 to –6.2) values, suggesting that these magmas were derived from an ancient crust-dominated source. Geochemical and Nd isotope data reveal that the peraluminous A_2-type rhyolites and biotite granites were derived by partial melting of felsic crustal rocks under low-pressure and high-temperature conditions. By integrating all the available data with the regional tectonic evolution of the southwestern Youjiang Basin and adjacent regions, we attribute the generation of the peraluminous A_2-type rhyolites and biotite granites to the extensional setting that existed during oceanic subduction, which was induced by roll-back of the Paleo-Tethys oceanic lithosphere at 251–249 Ma. This study indicates that subduction-related magmatism related to Paleo-Tethys oceanic lithosphere was still active in the early Triassic.

1. INTRODUCTION

The Triassic closure of the eastern branches of the Paleo-Tethys Ocean and associated backarc basins resulted in a vast composite continent in eastern and southeastern Asia, which comprises the North China Craton, South China Block (SCB), Indochina Block, Baoshan (Sibumasu) Block, and Qiangtang Block (Fig. 1; Metcalfe, 2011). The tectonic development of South China during this time involved large-scale intracontinental deformation and associated magmatism. The Triassic tectonic history of the southwestern SCB was affected by the Indosinian orogeny (Fromaget, 1941) and also records the amalgamation of the Indochina Block and SCB during the late Permian to Triassic due to closure of the eastern branch of the Paleo-Tethys Ocean (Cao et al., 2015; Halpin et al., 2016). However, subsequent studies have advocated that subduction of the Paleo-Pacific plate also occurred beneath the SCB in the late Permian and proposed a flat-slab subduction model followed by slab foundering to account for both the Indosinian orogeny and broad spatial distribution of the late Mesozoic magmatism (e.g., Li and Li, 2007; Li et al., 2012a). Although the origin and tectonic implications of the Mesozoic igneous rocks in South China have been extensively studied, the link between the Permian–Triassic igneous rocks in the southwestern SCB and a specific subduction zone is still controversial (Wang et al., 2021). The Mesozoic tectonomagmatism in the SCB is thought to be related to subduction in the Paleo-Tethys Ocean (Jiao et al., 2015; Li et al., 2016; Xu et al., 2018; Wang et al., 2020) or the Paleo-Pacific Ocean (Li et al., 2006, 2012b; Li and Li, 2007).

There are two Paleo-Tethys sutures, the Song Ma and Song Chay suture zones, between the Indochina Block and the SCB (Fig. 1). The Dian-Qiong suture (DQS) was identified by Cai and Zhang (2009). The western DQS approximately follows the China-Vietnam border, and the eastern DQS crosses Hainan Island (Fig. 1). The western DQS extends from Jianshui close to the Red River, through Babu and Napo, to Pingxiang in the China-Vietnam border area (Fig. 2A; Dong and Zhu, 1999; Wu et al., 1999, 2000, 2002). The DQS contains high- to ultrahigh-pressure metamorphic belts, early Carboniferous to early Permian ophiolites and mid-ocean ridge basalts, late Permian to early Triassic island-arc tholeiites and arc-related igneous rocks, and lower-middle Triassic sedimentary rocks (Li and Li, 2007; Cai et al., 2008; Cai and Zhang, 2009; Hu et al., 2012; Qiu et al., 2017; Li et al.,

XIJUN LIU https://orcid.org/0000-0002-7219-5914
*xijunliu@glut.edu.cn; liulei@glut.edu.cn

2019; Xiang et al., 2021). Analysis of these rocks has constrained the timing of opening and closure of the Paleo-Tethys Ocean and the subsequent accretional and collisional tectonic events. Widespread middle to late Triassic silicic igneous rocks along the suture can constrain the tectonic evolution of the continental crust and its magmatic history (Qi et al., 2007; Qin et al., 2018; Li et al., 2019). Gao et al. (2017) suggested that the ca. 240 Ma silicic magmatism in southwestern South China occurred during a tectonic transition from compression to extension but was mainly caused by extension. However, controversy remains regarding the timing of the evolution of the Paleo-Tethys, due to the variable ages and tectonic settings of the igneous rocks (Sun and Jian, 2004; Peng, 2006; Hennig et al., 2009; Zi et al., 2012a). Previous studies have proposed that subduction in the Paleo-Tethys Ocean started in the early Permian (Li, 2014; Wang et al., 2018a) and that the ocean closed during the middle Triassic (Zi et al., 2012a; Wang et al., 2018a). Other evidence from volcanic rocks suggests that subduction along the suture zone occurred during the early Permian–middle Triassic, followed by collision (Xin, 2018; Xin et al., 2018). Therefore, the early Triassic igneous rocks along the suture can provide clues to the subduction and collisional processes prior to closure of the Paleo-Tethys Ocean.

Many of the Permian–earliest Triassic igneous rocks along the Ailaoshan–Song Ma suture zones

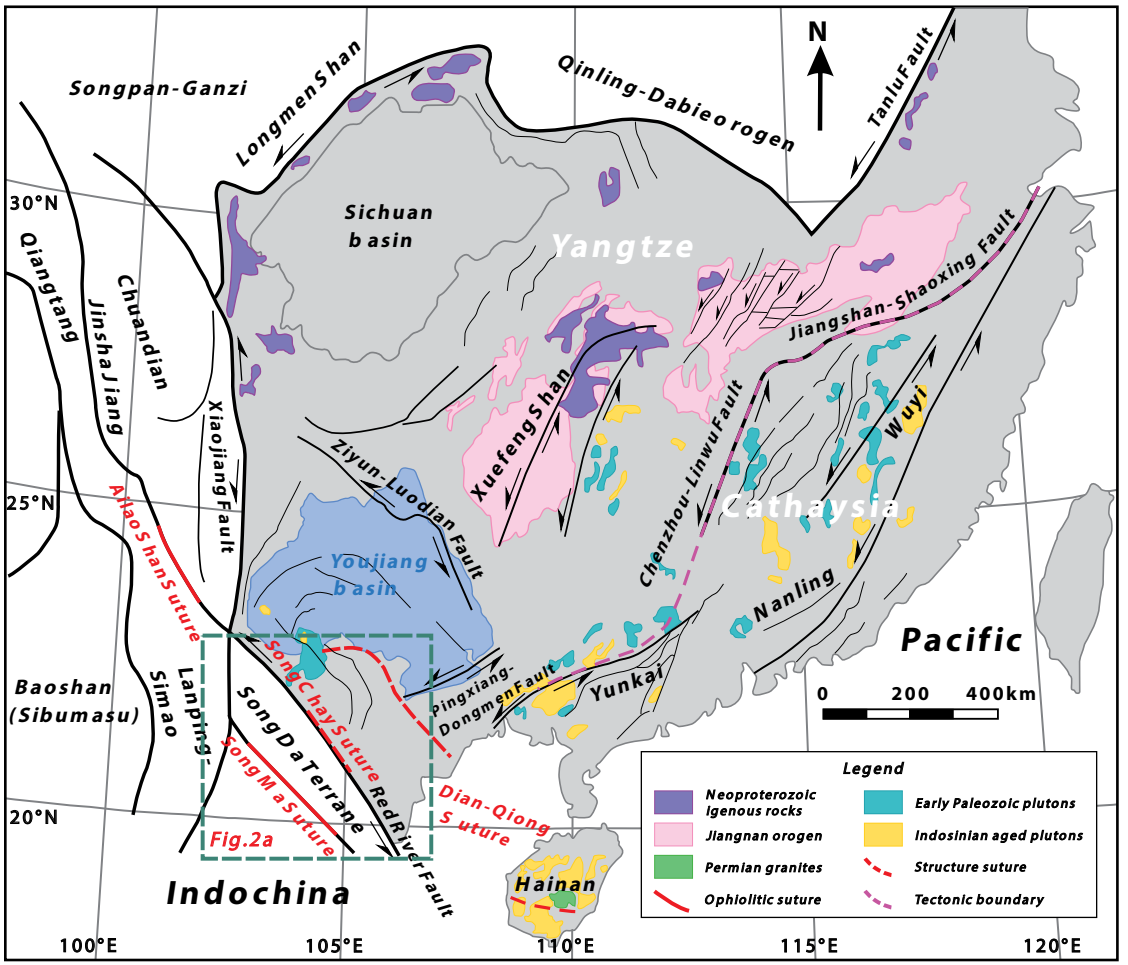

Figure 1. Simplified geological map of the South China Block (SCB) and adjacent tectonic units, showing the locations of the Youjiang Basin and the study area (modified after Duan et al., 2020).

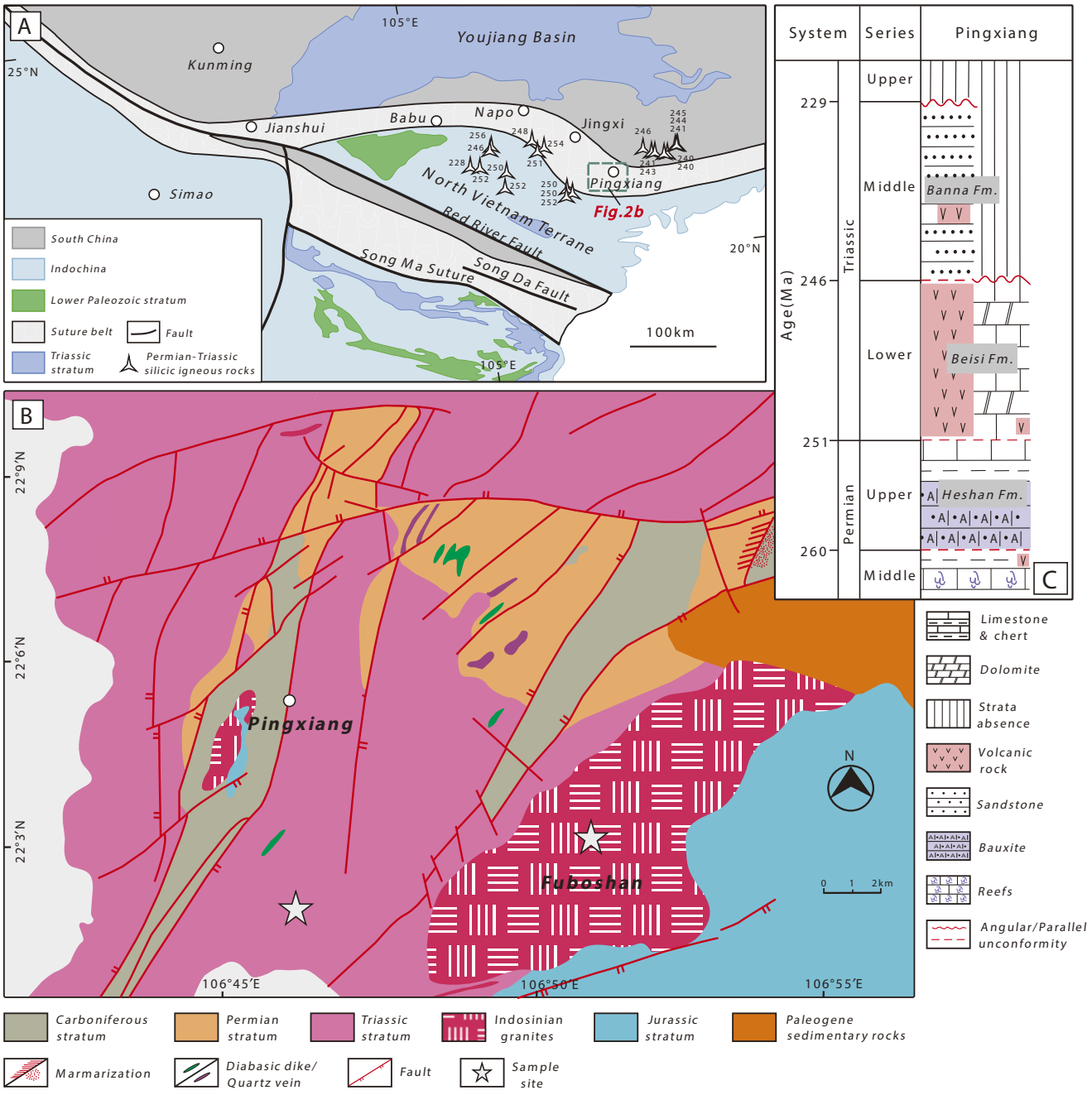

Figure 2. (A) Structural map showing the juxtaposition of the South China, Indochina, Simao, and Sibumasu blocks (after Cai and Zhang, 2009). Spatial-temporal distribution of Permian–Triassic silicic igneous rocks across the Dian-Qiong suture (DQS) are from Gan et al. (2021). (B) Simplified geological map and (C) stratigraphy of the Pingxiang area (modified after Wang et al., 2020).

have arc geochemical signatures with marked negative Nb-Ta anomalies, which indicate a subduction setting related to convergence of the SCB and Indochina Block (Zi et al., 2012b; Lai et al., 2014; Liu et al., 2015; Wang et al., 2018b). The Permian–Triassic igneous rocks along the DQS are only exposed in the southwestern Youjiang Basin where they occur in the lower-middle Triassic Beisi and Banba formations (Fig. 2; e.g., Wang and Deng, 2003; Qin et al., 2011, 2012; Li et al., 2019; Gan et al., 2021). The age and petrogenesis of these igneous rocks have only been constrained in limited areas of this region (Wang and Deng, 2003; Qin et al., 2011, 2012; Li et al., 2019; Gan et al., 2021). The basalts, rhyolites, dacites, and granites in the Ningming, Pingxiang, and Chongzuo areas along the southwestern margin of the Youjiang Basin formed from 256 Ma to 241 Ma during the early to middle Triassic and exhibit subduction-related arc-like geochemical features that are thought to be related to subduction in the Paleo-Tethys Ocean or syn- or post-collisional processes between the SCB and Indochina Block (Wang and Deng, 2003; Qin et al., 2011, 2012; Li et al., 2019; Gan et al., 2021). As such, the age and petrogenesis of the Permian–Triassic silicic igneous rocks in the Youjiang Basin need to be further constrained and may provide new insights into the tectonic evolution of the Paleo-Tethys Ocean between the SCB and Indochina Block (Wang and Deng, 2003; Qin et al., 2011; Gan et al., 2021).

In this paper, we report whole-rock major- and trace-element, whole-rock Nd and zircon Hf isotope, and zircon U-Pb age data for newly discovered peraluminous A_2-type rhyolites and biotite granites from the Pingxiang region, Guangxi Province, southwest China. We use these data to constrain the petrogenesis and tectonic setting of these rocks, which provide new insights into the tectonic evolution of the Paleo-Tethys Ocean during the Triassic.

2. GEOLOGICAL SETTING

South China is a continental terrane that is bounded to the north by the Qinling-Dabie collisional orogenic belt, to the east by the Pacific plate, and to the south by the Indochina Block (Fig. 1; Li et al., 2017). It is a collage consisting of the Yangtze Block in the northwest and Cathaysia Block in the southeast, which were amalgamated during the Neoproterozoic (860–820 Ma) along the Jiangshan-Shaoxing fault (Fig. 1; Li et al., 2009; Zhao, 2015; Xia et al., 2018; Yao et al., 2019). The Youjiang Basin is located at the southwestern margin of the SCB (Fig. 1) and is generally considered to have developed between the early Devonian and late Triassic, associated with the evolution of the Paleo-Tethys Ocean (Du et al., 2013; Hu et al., 2017). The Pingxiang area is located at the southwestern margin of the Youjiang Basin in the western DQS (Fig. 1). In this area, the combined effects of the coastal Pacific and Tethys tectonic domains resulted in frequent marine transgressions and regressions, intense magmatism, and a complex geological history.

Carboniferous to Paleogene strata are exposed in the Pingxiang area, but the Triassic rocks are most widely exposed (Fig. 2B). Based on the paleontology, contact relationships, and lithological features, the Triassic strata can be divided into a lower and middle series. The middle Triassic Banna Formation consists of sandstone. The lower Triassic Beisi Formation consists mainly of dolomite and volcanic rocks (Fig. 2C). There were two stages of magmatism in the area: Variscan (i.e., late Paleozoic) mafic volcanic rocks in the Naxiao-Shangshi area and Indosinian (i.e., early Mesozoic) large-scale silicic volcanic and intrusive rocks. During subduction in the Tethys oceans, a high heat flow has led to partial melting of the upper mantle. Subsequently, the upwelling of mantle-derived mafic magmas caused partial melting of the crust, which generated a series of intermediate-silicic magmas in an active continental margin tectonic setting.

The Pingxiang region contains large areas of Triassic volcanic rocks and a granitic pluton that intruded Triassic strata in the Fuboshan area, along with scarce mafic dikes in the Permian and Triassic strata (Fig. 2B). Triassic sedimentary rocks and dacites in the Pingxiang area (Qin et al., 2011; Song et al., 2014; Li et al., 2019) formed in an island arc–extinct backarc basin system. In this study, we investigated granites of the Fuboshan pluton, which occur as a NE-SW–trending oval-shaped batholith with a length of 14 km and width of 3–8 km. The pluton is mainly exposed in Shangshi town and Banwang village of Pingxiang city, where porphyritic biotite granite and granite porphyry crop out. Rhyolites in this area crop out near the Fuboshan pluton and are mainly exposed in Madong village and Xiashi town of Pingxiang city.

3. PETROGRAPHY

Representative samples of igneous rocks were collected from the Pingxiang area (Figs. 3A, 3D, and 3G), including biotite granite and rhyolite. The petrography of the samples is described below.

The biotite granite (sample 19-px-4) is gray, medium grained (Figs. 3A and 3B), and contains 25–30 vol% plagioclase, 5–10 vol% K-feldspar, 35–40 vol% quartz, 3–5 vol% biotite, and accessory minerals (<5 vol%) (Fig. 3C).

The rhyolites (samples 19-px-9 and -10) are gray and porphyritic (Figs. 3E and 3H). The phenocrysts are mainly quartz (20–30 vol%) and plagioclase (10–15 vol%), along with accessory minerals such as epidote (<3 vol%). The plagioclase is subhedral and exhibits polysynthetic twinning. The quartz grains are generally rounded and have embayed margins (Figs. 3F and 3I).

4. ANALYTICAL METHODS

All analyses were carried out at the Guangxi Key Laboratory of Hidden Metallic Ore Deposit Exploration, Guilin University of Technology, Guilin, China (Liu et al., 2020).

4.1. Zircon U-Pb Dating

Zircon crystals were extracted from rock samples by conventional crushing, heavy liquid, and magnetic separation techniques, and then hand-picking. Cathodoluminescence (CL) images of the crystals were used to examine their internal structures and select sites for U-Pb dating. In situ U-Pb dating was undertaken by laser ablation–inductively

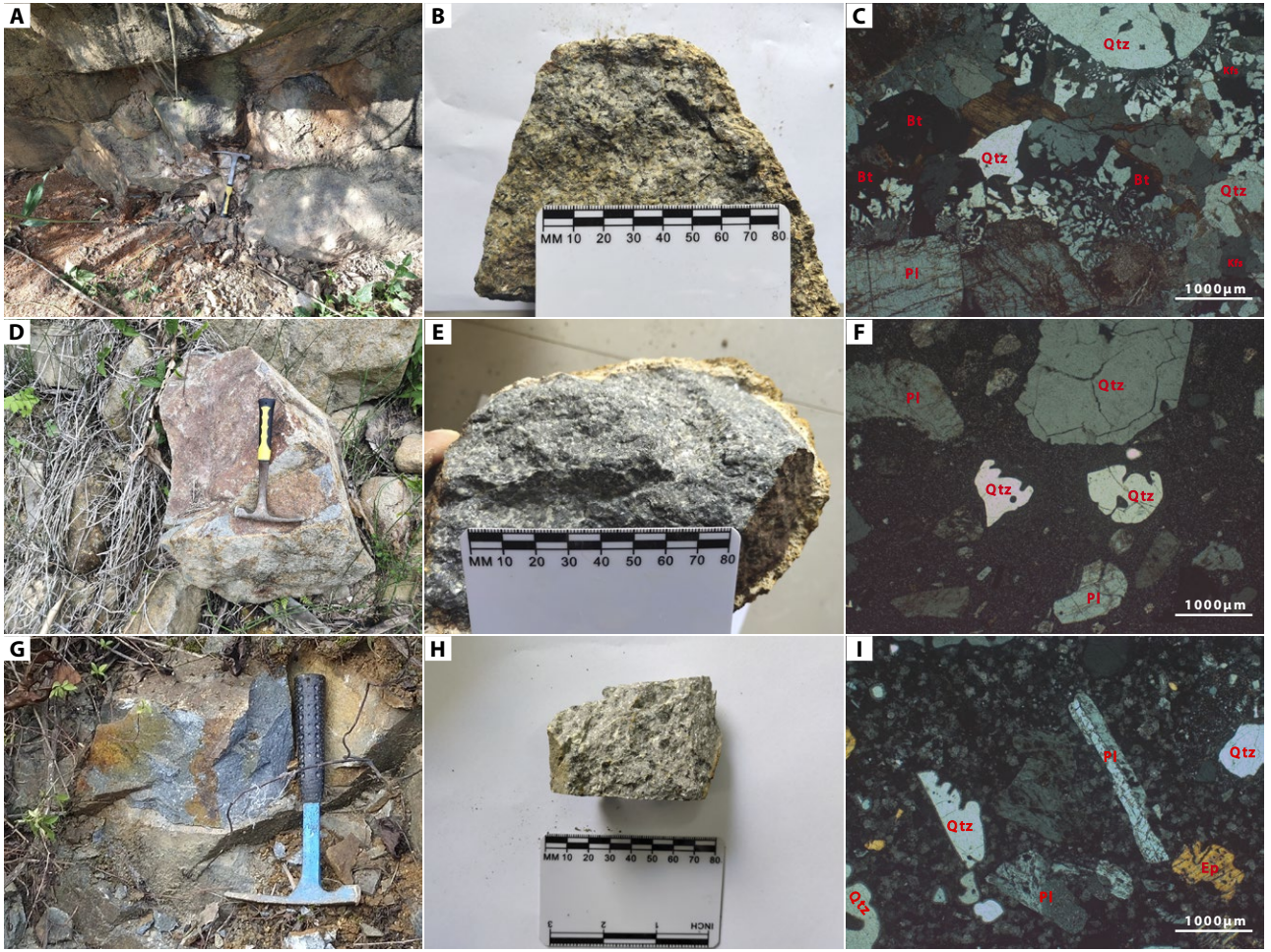

Figure 3. (A) Field photograph, (B) hand specimen, and (C) photomicrograph of the granite. (D and G) Field photographs, (E and H) hand specimens, and (F and I) photomicrographs of the rhyolites. Qtz—quartz; Kfs—K-feldspar; Pl—plagioclase; Bt—biotite; Ep—epidote.

coupled plasma–mass spectrometry (LA-ICP-MS). Helium was used as a carrier gas to enhance aerosol transport to the ICP source and to minimize aerosol deposition. Argon was used as the makeup gas and was mixed with the carrier gas. Nitrogen was added into the central gas flow (Ar + He) of the Ar plasma to reduce the detection limits and improve the precision (Hu et al., 2008; Liu et al., 2010b). Each analysis comprised 15–20 s of background data acquisition and 50 s of data acquisition during ablation, with a laser spot size and depth of 40 μm and 20–40 μm, respectively. The zircon 91500 (weighted-mean $^{206}Pb/^{238}U$ age = 1062 ± 6 Ma) and GJ-1 (weighted-mean $^{206}Pb/^{238}U$ age = 600 ± 4 Ma) standards were used to monitor the data quality. A detailed description of the analytical instrumentation and procedures was given by Yuan et al. (2008). In-house software ICPMSDataCal (Liu et al., 2010a) was used for off-line data selection, integration of background and analytical signals, time-drift corrections, and quantitative calibration of the U-Pb dating. Isoplot software was used for plotting the concordia and weighted-mean age diagrams (Ludwig, 2003).

4.2. Whole-Rock Major- and Trace-Element Analyses

Fresh rock samples were collected, and weathered surfaces were avoided or removed. The samples were first crushed into small chips that were powdered in an alumina ceramic shatter box. After fusion with lithium metaborate–lithium tetraborate flux and the oxidizing agent lithium nitrate, the products were poured into a platinum mold to generate a fused disk for major-element analysis by X-ray fluorescence spectrometry. Loss-on-ignition (LOI) values of each sample were measured after heating to 1000 °C. Trace-element analyses were undertaken with an Agilent 7900CX ICP-MS instrument after acid dissolution of the samples. About 12 mg of sample powder and standard samples were dissolved in a mixture of HNO_3, HCl, and HF. The U.S. Geological Survey standards BHVO, AGV, W-2, and G-2 and Chinese national rock standards (GSR-1, -2, and -3) were analyzed to monitor the data quality. Pure elemental standards were used for external calibration. The sample solutions were placed in clean plastic centrifuge tubes and analyzed by ICP-MS (Liu et al., 2020). The analytical precision was better than ±5% for major elements and better than ±2%–5% for most trace elements.

4.3. Whole-Rock Nd Isotope Analyses

Whole-rock powders for Nd isotope analysis were dissolved in Savillex Teflon capsules with 2 mL of 22 N HF and 1 mL of 8N HNO_3 at 120 °C on a hot plate for 5–7 d. After drying the sample, 3 mL of HNO_3 was added for 2 d to dissolve the samples. Neodymium was purified with HDEHP resin. Neodymium isotope ratios were measured with a Neptune Plus multi-collector (MC)-ICP-MS instrument. During the analysis period, the Sm-Nd blanks were <100 pg. The isotope ratios were normalized to $^{146}Nd/^{144}Nd = 0.7219$ to correct for instrumental mass fractionation. During the analysis period, data quality was assessed by analyzing the international standard JNdi-1. The JNdi-1 Nd standard yielded $^{143}Nd/^{144}Nd = 0.512081 \pm 0.000008$ (n = 40; 2 SD). The U.S. Geological Survey reference material BHVO-2 was analyzed to monitor the data accuracy and yielded $^{143}Nd/^{144}Nd = 0.512965 \pm 0.000004$ (Liu et al., 2020).

4.4. Zircon Lu-Hf Isotope Analyses

Zircon Lu-Hf isotope analyses were carried out with a Neptune Plus MC-ICP-MS coupled to an ArF excimer LA system. Instrument settings and analytical procedures were described by Wu et al. (2006) and Geng et al. (2011). The analyses were obtained on the same spots or domains as used for U-Pb dating. The analytical conditions were as follows: laser beam diameter = 44 μm, laser repetition rate = 6 Hz, and laser ablation time = 30 s. The zircon standard GJ-1 yielded a weighted-mean $^{176}Hf/^{177}Hf$ ratio of 0.282333 (n = 93). The present-day chondritic ratios of $^{176}Hf/^{177}Hf = 0.282772$ and $^{176}Lu/^{177}Hf = 0.0332$ were used to calculate $\varepsilon_{Hf}(t)$ values (Blichert-Toft and Albarède, 1997).

5. RESULTS

5.1. Zircon U-Pb Geochronology

A biotite granite sample (sample 19-PX-4) and two rhyolite samples (19-PX-9 and 19-PX-10) were chosen for zircon U-Pb dating (Table 1). Zircon grains from the biotite granite and rhyolites are colorless or bright in color and transparent to translucent. The zircon grains are mostly euhedral and long-prismatic crystals. The zircon grains are 70–130 μm in size and exhibit well-developed oscillatory zoning in CL images (Fig. 4), indicating a magmatic origin (Hoskin and Schaltegger, 2003).

5.1.1. Biotite Granite

Twenty-eight analyses of 28 zircons from the biotite granite yielded a weighted-mean $^{206}Pb/^{238}U$ age of 249 ± 1 Ma (mean square of weighted deviates [MSWD] = 0.16) (Fig. 4A). Zircon grains from the biotite granite have U contents of 378–1758 ppm and Th contents of 185–1365 ppm, with Th/U ratios of 0.20–0.78. The euhedral crystal morphology and oscillatory zoning suggest that 249 ± 1 Ma represents the crystallization age of the granite.

5.1.2. Rhyolites

Sixty-five zircon analyses of the rhyolites plot on the concordia (Figs. 4B and 4C). Thirty-five zircons from sample 19PX-9 contain 92–764 ppm Th and 563–2014 ppm U, with Th/U = 0.11–0.54. These values are typical of igneous zircons. The 35 analyses are concordant and yielded a weighted-mean $^{206}Pb/^{238}U$ age of 251 ± 1 Ma (Fig. 4B; MSWD = 0.25).

Thirty zircons from sample 19-PX-10 have high Th/U ratios (0.24–0.56), indicative of a magmatic origin. Most of these zircons are characterized by steep and heavy rare-earth element (REE)–enriched patterns with obvious negative Eu and positive Ce anomalies (Figs. 5B, 5D, and 5F), which are also indicative of a magmatic origin (Hoskin and Ireland, 2000; Hoskin and Schaltegger, 2003). Thirty analyses plot on the concordia (Fig. 4C) and yielded a weighted-mean $^{206}Pb/^{238}U$ age of 250 ± 1 Ma (MSWD = 0.12) (Fig. 4C), which is consistent with the age of sample 19-PX-9 (Table 1; Fig. 4B). As such, the crystallization ages of the rhyolite are ca. 250 Ma.

5.2. Whole-Rock Major- and Trace-Element Data

Whole-rock major- and trace-element data for seven rhyolites and five biotite granites from the Pingxiang area along the southwestern SCB are presented in Table 2 and Figures 5 and 6. The rhyolites have relatively high contents of SiO_2 (71.4–74.2 wt%) and K_2O (4.1–5.5 wt%) and relatively low contents of TiO_2 (0.4–0.5 wt%), MgO (0.4–0.7 wt%), and CaO (0.3–1.6 wt%). The data are plotted in the rhyolite field in Figure 5A, and all samples belong to the high-K calc-alkaline series (Figs. 5B and 5C) and are strongly peraluminous, with A/CNK values (molar $Al_2O_3/[CaO + Na_2O + K_2O]$) of 1.05–1.36 (Fig. 5D). The rhyolites have low $Mg^{\#}$ values (20–28) and Na_2O/K_2O ratios of 0.34–0.51 (except for a sample with a value of 0.72). The rhyolites are light REE–enriched with $(La/Yb)_N$ ($_N$ indicates normalization

TABLE 1. ZIRCON U-Pb ISOTOPE DATA FOR THE PINGXIANG RHYOLITIC AND BIOTITE GRANITIC SAMPLES

Sample	Pb	Th	U	$^{207}Pb/^{206}Pb$		$^{207}Pb/^{235}U$		$^{206}Pb/^{238}U$		$^{207}Pb/^{235}U$		$^{206}Pb/^{238}U$	
		ppm		Ratio	1Σ	Ratio	1Σ	Ratio	1Σ	Age (Ma)	1Σ	Age (Ma)	1Σ
19px-4-1	31	369	649	0.06088	0.00227	0.2837	0.0133	0.03938	0.00043	292	10	249	3
19px-4-2	24	185	528	0.05143	0.00174	0.2777	0.0093	0.03927	0.00044	249	7	248	3
19px-4-3	25	229	553	0.04693	0.00153	0.2616	0.0079	0.03908	0.00037	228	6	247	2
19px-4-4	35	261	791	0.05199	0.00157	0.2848	0.0106	0.03933	0.00050	254	8	249	3
19px-4-5	29	287	641	0.04712	0.00142	0.2635	0.0076	0.03914	0.00036	229	6	248	2
19px-4-6	31	322	676	0.05006	0.00155	0.2721	0.0088	0.03932	0.00036	244	7	249	2
19px-4-7	36	365	791	0.04890	0.00150	0.2631	0.0079	0.03920	0.00033	237	6	248	2
19px-4-8	28	296	624	0.04922	0.00147	0.2675	0.0081	0.03949	0.00040	241	7	250	2
19px-4-9	29	347	622	0.05183	0.00172	0.2797	0.0093	0.03923	0.00034	250	7	248	2
19px-4-10	25	245	536	0.05720	0.00208	0.2790	0.0115	0.03903	0.00036	273	9	247	2
19px-4-11	26	238	563	0.05013	0.00157	0.2721	0.0085	0.03930	0.00035	244	7	248	2
19px-4-12	75	970	1554	0.04942	0.00113	0.2692	0.0059	0.03940	0.00024	242	5	249	2
19px-4-13	18	259	378	0.05000	0.00218	0.2677	0.0110	0.03916	0.00045	241	9	248	3
19px-4-14	18	188	395	0.04652	0.00182	0.2593	0.0101	0.03932	0.00040	226	8	249	2
19px-4-15	24	241	522	0.04679	0.00175	0.2774	0.0099	0.03912	0.00037	224	8	247	2
19px-4-16	89	1365	1758	0.04441	0.00130	0.2674	0.0084	0.03949	0.00034	216	7	250	2
19px-4-17	33	349	697	0.04812	0.00174	0.2539	0.0109	0.03917	0.00039	230	9	248	2
19px-4-18	68	998	1345	0.05126	0.00179	0.2774	0.0115	0.03944	0.00034	249	9	249	2
19px-4-19	42	451	909	0.04637	0.00154	0.2659	0.0085	0.03911	0.00031	223	7	247	2
19px-4-20	26	287	570	0.04939	0.00177	0.2624	0.0096	0.03926	0.00039	237	8	248	2
19px-4-21	31	331	666	0.05214	0.00167	0.2811	0.0096	0.03937	0.00037	252	8	249	2
19px-4-22	24	282	513	0.04837	0.00163	0.2773	0.0086	0.03914	0.00041	232	7	248	3
19px-4-23	22	223	490	0.04789	0.00161	0.2674	0.0091	0.03934	0.00039	233	7	249	2
19px-4-24	62	294	1434	0.04498	0.00113	0.2621	0.0067	0.03941	0.00032	220	5	249	2
19px-4-25	22	201	479	0.04668	0.00182	0.2593	0.0099	0.03938	0.00036	226	8	249	2
19px-4-26	32	289	717	0.04578	0.00148	0.2548	0.0088	0.03929	0.00033	222	7	248	2
19px-4-27	30	312	638	0.04281	0.00155	0.2687	0.0089	0.03959	0.00036	209	7	250	2
19px-4-28	30	303	651	0.04555	0.00167	0.2730	0.0099	0.03947	0.00039	221	8	250	2
19px-9-1	61	396	1365	0.04697	0.00136	0.2660	0.0085	0.03972	0.00044	231	7	251	3
19px-9-2	44	400	962	0.04668	0.00145	0.2644	0.0085	0.03992	0.00046	230	7	252	3
19px-9-3	44	230	1002	0.04836	0.00141	0.2728	0.0082	0.03966	0.00038	237	7	251	2
19px-9-4	62	383	1418	0.04737	0.00126	0.2685	0.0073	0.03980	0.00032	233	6	252	2
19px-9-5	78	251	1850	0.04713	0.00109	0.2666	0.0063	0.03969	0.00029	232	5	251	2
19px-9-6	53	351	1194	0.04637	0.00122	0.2642	0.0069	0.03994	0.00028	230	6	252	2
19px-9-7	58	350	1336	0.04849	0.00134	0.2646	0.0076	0.03974	0.00030	238	6	251	2
19px-9-8	50	187	1186	0.04611	0.00135	0.2700	0.0075	0.03958	0.00033	227	6	250	2
19px-9-9	59	248	1378	0.04458	0.00117	0.2529	0.0067	0.03984	0.00029	221	5	252	2
19px-9-10	49	290	1127	0.04639	0.00140	0.2710	0.0080	0.03967	0.00028	227	6	251	2
19px-9-11	61	303	1413	0.04295	0.00112	0.2536	0.0069	0.03987	0.00028	213	6	252	2
19px-9-12	58	275	1327	0.04528	0.00146	0.2539	0.0091	0.03977	0.00028	222	7	251	2
19px-9-13	88	447	2014	0.04214	0.00131	0.2554	0.0085	0.03962	0.00028	206	7	250	2
19px-9-14	43	285	959	0.04492	0.00168	0.2600	0.0107	0.03979	0.00036	218	9	252	2
19px-9-15	53	368	1158	0.04206	0.00138	0.2661	0.0087	0.03996	0.00031	207	7	253	2
19px-9-16	52	303	1186	0.04372	0.00142	0.2524	0.0087	0.03947	0.00032	212	7	250	2
19px-9-17	39	253	883	0.04580	0.00164	0.2742	0.0097	0.03966	0.00033	222	8	251	2
19px-9-18	71	446	1598	0.04447	0.00133	0.2771	0.0083	0.03947	0.00028	216	7	250	2
19px-9-19	50	367	1106	0.04713	0.00161	0.2642	0.0100	0.03980	0.00031	230	8	252	2

(*continued*)

TABLE 1. ZIRCON U-Pb ISOTOPE DATA FOR THE PINGXIANG RHYOLITIC AND BIOTITE GRANITIC SAMPLES (*continued*)

Sample	Pb	Th	U	$^{207}Pb/^{206}Pb$		$^{207}Pb/^{235}U$		$^{206}Pb/^{238}U$		$^{207}Pb/^{235}U$		$^{206}Pb/^{238}U$	
		ppm		Ratio	1Σ	Ratio	1Σ	Ratio	1Σ	Age (Ma)	1Σ	Age (Ma)	1Σ
19px-9-20	28	230	625	0.04454	0.00172	0.2566	0.0102	0.03933	0.00034	216	8	249	2
19px-9-21	37	92.3	875	0.04607	0.00167	0.2572	0.0104	0.03961	0.00032	224	8	250	2
19px-9-22	35	351	714	0.05930	0.00242	0.2918	0.0150	0.03988	0.00035	283	12	252	2
19px-9-23	48	345	1064	0.04482	0.00149	0.2509	0.0091	0.03967	0.00030	219	7	251	2
19px-9-24	44	186	1002	0.04735	0.00147	0.2638	0.0087	0.03959	0.00028	230	7	250	2
19px-9-25	32	240	707	0.04522	0.00156	0.2535	0.0094	0.03974	0.00035	221	8	251	2
19px-9-26	42	254	936	0.04603	0.00145	0.2755	0.0086	0.03931	0.00030	223	7	249	2
19px-9-27	46	342	1014	0.04546	0.00153	0.2549	0.0095	0.03967	0.00033	222	8	251	2
19px-9-28	67	408	1475	0.04478	0.00129	0.2733	0.0080	0.03992	0.00028	221	6	252	2
19px-9-29	85	398	1927	0.04537	0.00118	0.2565	0.0074	0.03975	0.00030	224	6	251	2
19px-9-30	53	237	1201	0.04592	0.00123	0.2782	0.0072	0.03963	0.00033	225	6	251	2
19px-9-31	68	764	1414	0.04819	0.00130	0.2719	0.0074	0.03970	0.00027	236	6	251	2
19px-9-32	36	278	784	0.04952	0.00152	0.2803	0.0087	0.03990	0.00040	243	7	252	2
19px-9-33	57	482	1243	0.04667	0.00115	0.2654	0.0065	0.03978	0.00027	231	5	251	2
19px-9-34	26	216	563	0.04828	0.00158	0.2725	0.0086	0.03957	0.00035	237	7	250	2
19px-9-35	42	344	918	0.04900	0.00120	0.2888	0.0067	0.03979	0.00036	242	5	252	2
19px-10-1	33	356	700	0.05044	0.00171	0.2838	0.0092	0.03966	0.00037	246	7	251	2
19px-10-2	41	221	938	0.04856	0.00148	0.2655	0.0085	0.03971	0.00046	239	7	251	3
19px-10-3	28	260	620	0.04665	0.00181	0.2605	0.0095	0.03946	0.00040	227	8	249	2
19px-10-4	25	241	554	0.04626	0.00160	0.2517	0.0089	0.03965	0.00035	228	7	251	2
19px-10-5	32	341	711	0.04395	0.00147	0.2379	0.0083	0.03955	0.00039	217	7	250	2
19px-10-6	39	380	868	0.04642	0.00153	0.2501	0.0085	0.03949	0.00036	227	7	250	2
19px-10-7	26	237	565	0.04413	0.00167	0.2597	0.0094	0.03978	0.00035	218	8	251	2
19px-10-8	14	131	307	0.04506	0.00194	0.2528	0.0102	0.03977	0.00044	221	8	251	3
19px-10-9	27	198	607	0.04631	0.00157	0.2610	0.0087	0.03965	0.00034	227	7	251	2
19px-10-10	22	199	479	0.04575	0.00163	0.2587	0.0090	0.03973	0.00038	225	7	251	2
19px-10-11	33	207	732	0.04648	0.00126	0.2618	0.0064	0.03961	0.00032	228	5	250	2
19px-10-12	34	329	711	0.04588	0.00112	0.2515	0.0062	0.03976	0.00030	228	5	251	2
19px-10-13	29	288	607	0.04711	0.00151	0.2546	0.0077	0.03954	0.00034	230	6	250	2
19px-10-14	49	431	1043	0.04590	0.00106	0.2597	0.0057	0.03941	0.00032	226	5	249	2
19px-10-15	59	345	1296	0.04855	0.00172	0.2643	0.0089	0.03948	0.00041	238	7	250	3
19px-10-16	29	275	626	0.04794	0.00129	0.2616	0.0069	0.03957	0.00032	236	6	250	2
19px-10-17	20	112	441	0.04845	0.00156	0.2630	0.0084	0.03941	0.00036	237	7	249	2
19px-10-18	28	276	594	0.04788	0.00140	0.2601	0.0075	0.03947	0.00034	235	6	250	2
19px-10-19	20	185	438	0.05086	0.00159	0.2776	0.0086	0.03980	0.00040	249	7	252	2
19px-10-20	48	554	989	0.04900	0.00108	0.2687	0.0060	0.03963	0.00028	242	5	251	2
19px-10-21	26	264	567	0.04876	0.00155	0.2661	0.0086	0.03941	0.00033	240	7	249	2
19px-10-22	27	255	573	0.05042	0.00143	0.2742	0.0076	0.03952	0.00031	246	6	250	2
19px-10-23	33	323	701	0.05022	0.00142	0.2735	0.0073	0.03963	0.00029	245	6	251	2
19px-10-24	25	257	530	0.04866	0.00165	0.2649	0.0085	0.03977	0.00036	239	7	251	2
19px-10-25	26	252	556	0.04885	0.00143	0.2672	0.0080	0.03961	0.00034	240	6	250	2
19px-10-26	29	211	655	0.04950	0.00129	0.2702	0.0071	0.03955	0.00032	243	6	250	2
19px-10-27	30	283	653	0.05068	0.00136	0.2872	0.0074	0.03961	0.00029	248	6	250	2
19px-10-28	39	241	887	0.05037	0.00120	0.2748	0.0065	0.03957	0.00029	247	5	250	2
19px-10-29	38	412	802	0.05029	0.00125	0.2761	0.0071	0.03971	0.00030	248	6	251	2
19px-10-30	28	290	596	0.05303	0.00164	0.2815	0.0090	0.03980	0.00031	260	7	252	2

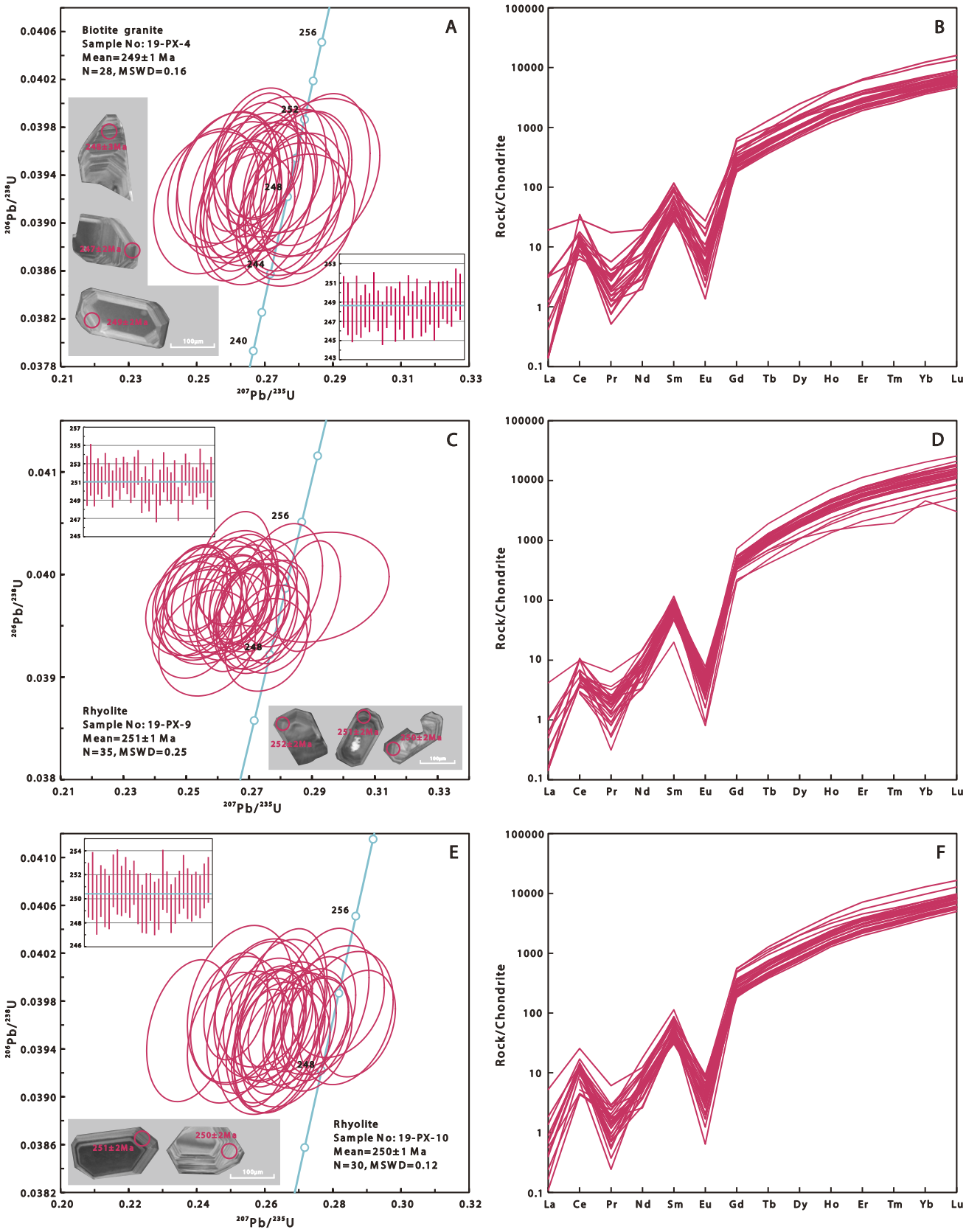

Figure 4. Zircon U-Pb dating results for the rhyolites and biotite granites. (A, C, and E) Zircon U-Pb concordia diagrams and cathodoluminescence images; (B, D, and F) zircon chondrite-normalized rare-earth element (REE) patterns. MSWD—mean square of weighted deviates.

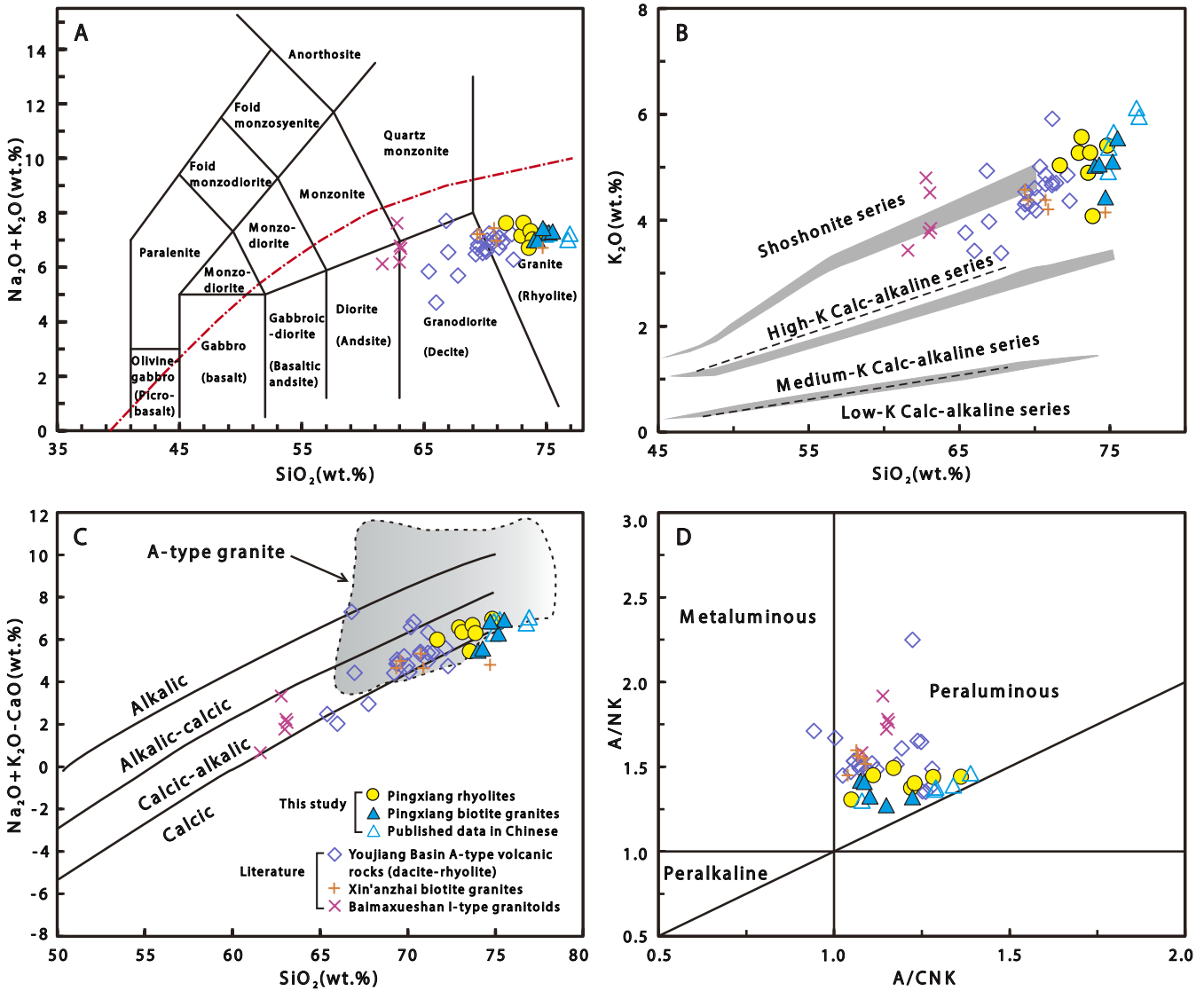

Figure 5. Major-element plots for the rhyolites and biotite granites. (A) $Na_2O + K_2O$ versus SiO_2 (after Wilson, 1989); (B) K_2O versus SiO_2; (C) $Na_2O + K_2O$–CaO versus SiO_2 (after Frost et al., 2001); (D) A/NK [molar ratio $Al_2O_3/(Na_2O + K_2O)$] versus A/CNK [molar ratio $Al_2O_3/(CaO + Na_2O + K_2O)$] (after Maniar and Piccoli, 1989). Data sources: published data are from Huang et al. (2022); Youjiang Basin silicic igneous rock data are from Gan et al. (2021); Xin'anzhai biotite granite data are from Yang et al. (2018); Baimaxueshan I-type granitoid data are from He et al. (2018).

TABLE 2. MAJOR- (wt%) AND TRACE- (ppm) ELEMENT DATA FOR THE PINGXIANG RHYOLITIC AND BIOTITE GRANITIC SAMPLES

Sample no.	Biotite granites					Rhyolites						
	19px-1	19px-2	19px-3	19px-4	19px-5	19px-6	19px-7	19px-8	19px-9	19px-10	19px-11	19px-12
Bulk element (wt%)												
SiO_2	75.2	75.5	74.0	74.3	74.7	71.7	72.9	74.8	73.1	73.7	73.9	73.6
TiO_2	0.42	0.42	0.47	0.48	0.48	0.47	0.51	0.52	0.50	0.49	0.41	0.52
Al_2O_3	12.1	11.8	12.3	12.2	12.4	14.0	12.7	12.8	12.3	12.5	13.0	12.3
Fe_2O_3T	3.51	3.99	4.02	4.05	3.42	3.72	5.25	3.75	4.50	4.57	4.20	4.82
MnO	0.05	0.09	0.07	0.07	0.06	0.08	0.06	0.06	0.08	0.07	0.07	0.08
MgO	0.40	0.45	0.54	0.48	0.85	0.62	0.73	0.41	0.52	0.65	0.66	0.61
CaO	1.01	0.39	1.51	1.41	0.57	1.62	0.59	0.28	1.27	0.63	0.72	1.26
Na_2O	2.18	1.77	1.96	1.93	3.00	2.58	1.89	1.85	2.05	2.04	2.94	1.81
K_2O	5.10	5.54	5.03	5.05	4.43	5.04	5.27	5.41	5.57	5.28	4.08	4.90
P_2O_5	0.08	0.08	0.10	0.10	0.10	0.14	0.11	0.10	0.11	0.11	0.09	0.10
LOI	0.81	1.27	0.67	0.76	1.06	1.29	1.14	1.42	1.65	1.16	0.87	3.09
Mg#	20.9	20.8	23.9	21.5	36.7	27.9	24.5	20.3	21.1	24.9	26.7	22.8
Trace element (ppm)												
V	14.3	21.8	25.6	63.0	44.6	28.8	28.7	26.1	24.8	23.9	15.3	22.2
Cr	6.60	7.40	5.80	7.20	2.10	1.60	5.79	3.49	1.67	5.07	2.84	4.92
Co	3.10	3.53	4.95	6.79	4.44	7.38	4.40	3.81	4.15	3.96	1.93	3.23
Ni	5.96	1.10	3.29	1.20	4.10	2.45	0.50	0.19	0.82	0.94	0.46	0.32
Cu	7.18	9.98	8.78	14.39	9.18	8.05	8.75	12.72	8.99	8.49	5.34	7.66
Zn	89.6	89.4	48.1	61.1	46.5	62.3	87.3	88.2	73.2	63.9	54.3	79.7
Ga	26.2	21.9	23.0	22.1	22.4	21.0	22.8	21.5	20.3	19.3	21.6	19.0
Rb	246	261	240	239	170	183	189	209	169	205	127	197
Sr	56.8	65.2	91.8	88.8	87.3	83.3	64.4	54.2	68.6	70.4	96.1	109
Y	60.8	59.6	63.4	57.7	56.0	36.9	54.1	60.6	47.0	50.5	50.5	58.2
Zr	265	266	247	272	301	238	263	231	227	261	258	263
Nb	15.6	13.7	14.4	15.7	14.3	9.47	14.4	13.7	12.8	14.1	12.9	13.9
Ta	1.15	1.49	1.44	1.41	1.44	1.01	1.55	1.48	1.34	1.26	1.28	1.29
Mo	1.53	1.17	1.84	2.19	2.84	1.32	0.65	0.73	1.02	0.80	0.67	0.79
Ba	864	858	990	902	688	793	838	926	744	850	954	819
La	68.8	57.4	61.8	58.6	48.1	41.2	50.6	49.9	43.2	51.5	37.5	51.8
Ce	95.4	90.4	115.4	111.0	92.8	80.0	100.3	99.3	86.4	101	81.8	94.8
Pr	15.8	15.0	16.1	14.6	12.4	9.93	12.9	13.0	11.2	12.4	10.6	12.7
Nd	67.0	58.6	63.6	57.5	48.9	38.0	51.0	52.7	44.4	47.9	41.7	49.4
Sm	15.3	12.5	13.4	12.0	10.5	7.71	10.8	11.3	9.36	9.67	9.10	10.3
Eu	2.27	1.76	2.00	1.75	1.64	1.24	1.77	1.94	1.50	1.55	1.01	1.53
Gd	16.5	13.5	14.2	13.0	11.5	8.01	12.3	13.0	10.5	9.89	9.45	10.9
Tb	2.24	2.19	2.32	2.07	1.90	1.29	1.99	2.11	1.69	1.64	1.63	1.80
Dy	15.3	12.2	13.0	11.8	10.8	7.23	11.2	12.0	9.56	9.62	9.83	10.7
Ho	2.08	2.39	2.57	2.35	2.19	1.41	2.24	2.43	1.92	1.92	1.98	2.16
Er	7.94	7.12	7.67	7.04	6.59	4.12	6.81	7.31	5.82	5.71	5.85	6.45
Tm	1.15	1.04	1.12	1.02	0.97	0.58	1.00	1.07	0.86	0.84	0.86	0.94
Yb	9.89	6.98	7.48	6.81	6.45	5.80	6.82	7.18	5.88	6.48	5.57	6.15
Lu	1.16	1.05	1.12	1.03	0.97	0.57	1.03	1.07	0.88	0.84	0.85	0.94
Hf	6.67	9.13	8.60	9.06	9.67	6.82	9.15	8.26	7.25	7.88	8.25	8.13
Th	24.5	25.1	27.9	25.8	24.2	22.9	25.3	24.0	21.4	23.4	27.6	22.9
U	5.45	5.98	5.27	4.92	5.47	4.80	5.80	5.35	4.88	4.99	6.16	5.04
Ti	2497	2499	2826	2850	2867	2820	3037	3089	3008	2964	2477	3110
Al	6.38	6.22	6.50	6.44	6.55	7.43	6.70	6.77	6.50	6.60	6.86	6.54
10,000 × Ga/Al	4.11	3.52	3.54	3.43	3.42	2.96	3.41	3.17	2.96	2.93	3.15	2.91
$(La/Yb)_N$	4.99	5.90	5.93	6.18	5.35	5.10	5.32	4.99	5.28	5.71	4.83	6.05
$(La/Sm)_N$	2.90	2.97	2.97	3.17	2.96	3.46	3.02	2.84	2.98	3.44	2.66	3.26
$(Gd/Yb)_N$	1.38	1.60	1.57	1.58	1.48	1.14	1.49	1.50	1.47	1.26	1.40	1.46
δEu	0.44	0.42	0.44	0.43	0.46	0.48	0.47	0.49	0.47	0.49	0.33	0.44

Notes: $Mg^{\#}$—molar Mg/(Mg + Fe)´100; LOI—loss on ignition.

to chondrite values) = 4.8–6.1 and have significant negative Eu anomalies (δEu = 0.33–0.49; Fig. 6A). The primitive-mantle–normalized multi-element patterns exhibit enrichments in Rb, Th, U, and Nd and depletions in Nb, Ta, Sr, and Ti (Fig. 6B).

The biotite granites plot in the granite field (Fig. 5A) and have SiO_2 = 73.6–74.8 wt%. They are high-K calc-alkaline rocks (Figs. 5B and 5C) and are weakly peraluminous with A/CNK = 1.08–1.22 (Fig. 5D). The biotite granites have high and variable total REE (ΣREE) concentrations of 256–330 ppm. In chondrite-normalized REE diagrams (Fig. 6C), the samples exhibit light REE enrichment relative to heavy REEs, with highly variable $(La/Yb)_N$ (5.0–6.2), $(La/Sm)_N$ (2.9–3.2), and $(Gd/Yb)_N$ (1.4–1.6) ratios as well as moderately negative Eu anomalies (δEu = 0.42–0.46). The biotite granites have trace-element compositions similar to those of middle–upper continental crust (Rudnick and Gao, 2003), with enrichments in Rb, Th, and U, and depletions in Ba, Sr, Nb, Ta, P, and Ti (Fig. 6D).

5.3. Neodymium-Hf Isotope Data

Whole-rock Nd isotope data are listed in Table 3. The biotite granites have enriched Nd isotopic

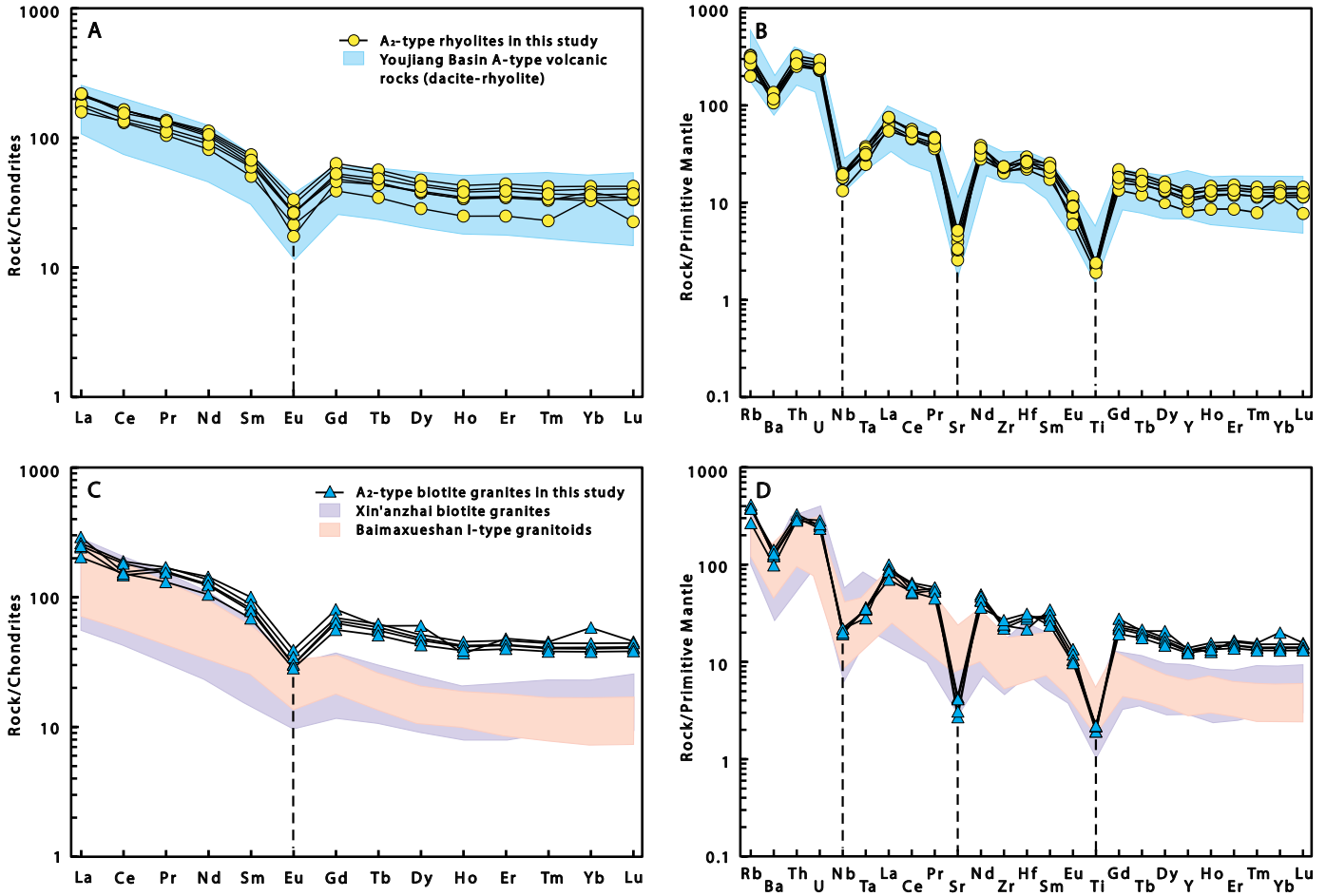

Figure 6. (A and C) Chondrite-normalized rare-earth element (REE) patterns and (B and D) primitive-mantle–normalized, trace-element diagrams for the rhyolites and biotite granites. Chondrite-normalizing values are from Boynton (1984), and primitive-mantle–normalizing values are from Sun and McDonough (1989).

TABLE 3. NEODYMIUM ISOTOPE DATA FOR THE PINGXIANG RHYOLITIC AND BIOTITE GRANITIC SAMPLES

Sample	Sm (ppm)	Nd (ppm)	$^{147}Sm/^{144}Nd$	$^{143}Nd/^{144}Nd$	2Σ	$(^{143}Nd/^{144}Nd)i$	$\varepsilon_{Nd}(t)$	T_{DM2} (Ma)
19px-2	12.5	58.6	0.1313	0.511996	0.000004	0.511783	–10.5	1879
19px-3	13.4	63.6	0.1298	0.511996	0.000005	0.511786	–10.4	1875
19px-4	12.0	57.5	0.1279	0.511991	0.000004	0.511784	–10.4	1878
19px-5	10.5	48.9	0.1320	0.511991	0.000006	0.511777	–10.6	1890
19px-6	7.71	38.0	0.1248	0.511929	0.000005	0.511724	–11.5	1970
19px-7	10.8	51.0	0.1307	0.511980	0.000004	0.511766	–10.7	1903
19px-8	11.3	52.7	0.1323	0.511977	0.000004	0.511761	–10.8	1912
19px-9	9.36	44.4	0.1298	0.511986	0.000005	0.511774	–10.6	1891
19px-10	9.67	47.9	0.1241	0.512022	0.000009	0.511819	–9.71	1820
19px-11	9.10	41.7	0.1341	0.512015	0.000005	0.511795	–10.1	1856
19px-12	10.3	49.4	0.1280	0.512019	0.000006	0.511809	–9.87	1834

Notes: Initial ratios were calculated assuming ages of 251–248 Ma for all samples. $(^{143}Nd/^{144}Nd)i$ = initial $^{143}Nd/^{144}Nd$ ratio.

compositions, with $\varepsilon_{Nd}(t)$ and T_{DM2}(Nd) values of –10.6 to –10.4 and ca. 1.9 Ga, respectively. The rhyolites have similar Nd isotopic compositions as the biotite granites, with $\varepsilon_{Nd}(t)$ and T_{DM2}(Nd) values of –11.5 to –9.7 and 1.8–2.0 Ga, respectively.

Zircon Hf isotope data are listed in Table 4. For the calculation of the $\varepsilon_{Hf}(t)$ and T_{DM2}(Hf) values, the in situ zircon U-Pb ages were used. The 253–249 Ma rhyolites have enriched zircon Hf isotopic compositions, with $\varepsilon_{Hf}(t)$ and T_{DM2}(Hf) values of –12.9 to –6.2 and 1.6–2.9 Ga, respectively. The 250–247 Ma biotite granites have similar zircon Hf isotopic compositions as the rhyolites, with variable $\varepsilon_{Hf}(t)$ (–14.5 to –6.7) and T_{DM2}(Hf) values (1.7–2.2 Ga).

6. DISCUSSION

6.1. Petrogenesis and Magma Sources

All the studied samples are fresh, and thin-section observations show that the samples are little affected by alteration. The samples have low LOI values (0.67–1.65 wt%, except for one rhyolite with a value of 3.09 wt%).

6.1.1. A-Type Affinity

Based on the nature of their protolith and the pressure-temperature of melting, silicic igneous rocks are generally subdivided into A-, I-, S-, and M-types (Bonin, 2007). Several geochemical approaches have been proposed to discriminate between A-type and other types of granites (Whalen et al., 1987; Eby, 1992), including high $Na_2O + K_2O$ contents, and Ga/Al and molar Fe/Mg ratios, low CaO contents, high-field-strength element (HFSE) enrichments, and Sr and Eu depletions (Whalen et al., 1987; Bonin, 2007). On Zr or Nb versus 10,000 × Ga/Al diagrams, the studied rhyolites and granites plot in the field for A-type granites (Figs. 7A and 7B; Whalen et al., 1987). Although highly fractionated I- and S-type granites can both have high FeO^T/MgO ratios, the rhyolites and biotite granites plot in the A-type field on a FeO^T/MgO versus (Zr + Nb + Ce + Y) diagram (Fig. 7C), which is generally used to distinguish A-type from highly differentiated I-type granites. It is generally accepted that A-type granites are derived from a relatively high-temperature magma chamber (>800 °C) that is usually at shallow crustal levels (Eby, 1990; King et al., 2001; Bonin, 2007). The calculated zircon saturation temperatures of the biotite granites and rhyolites are 835–870 °C (average = 860 °C), which further indicate their A-type nature. The A-type granites can be further subdivided into A_1- and A_2-type granites (Eby, 1992). On Rb/Nb versus Y/Nb, Nb-Y-Ce, and Nb-Y-3 × Ga diagrams (Figs. 7D–7F), all the studied rhyolites and biotite granites plot in the A_2-type field.

6.1.2. Petrogenesis of the A_2-Type Rhyolites and Biotite Granites

The ages of the studied rhyolites (251–250 Ma) and biotite granites (249 Ma) are the same within error, and these rocks have similar geochemical characteristics and isotopic compositions, indicating they were derived from a common magma source. In Harker diagrams (Fig. 8), Al_2O_3, P_2O_5, TiO_2, and $Fe_2O_3^T$ contents exhibit negative correlations with SiO_2, suggestive of fractionation of K-feldspar, plagioclase, biotite, apatite, and Fe-Ti oxides. On the basis of the available data, the biotite granites have a petrogenetic link with the coexisting rhyolites, and the biotite granites are more fractionated than the rhyolites (Fig. 8). Therefore, we propose that the biotite granites and rhyolites were cogenetic and formed by the fractional crystallization of the same parental magma, representing crystal cumulates and residual melts, respectively.

In general, A-type granites can be generated by three mechanisms: (1) direct fractionation of mantle-derived basaltic magmas (Turner et al., 1992; Mushkin et al., 2003), (2) hybridization of crust-derived silicic and mantle-derived mafic magmas (Kemp et al., 2005; Yang et al., 2006), and (3) partial melting of a variety of crustal materials at high temperatures and low pressures (Landenberger and Collins, 1996; Dall'Agnol and de Oliveira, 2007). If the studied A_2-type rhyolites and biotite granites were generated by extreme differentiation of mantle-derived basaltic magmas, the volume of mafic magma intruded into the upper crust should be an order of magnitude greater than that of the rhyolite and granite (Turner et al., 1992; Frost et al., 2001). However, the early Triassic volcanic and intrusive rocks in the Pingxiang area are dominated by rhyolitic and granitic rocks (Fig. 2B). The rhyolites and biotite granites are characterized by negative Nb and Ta anomalies (Figs. 6B and 6D), high SiO_2 contents, and low MgO, FeO^T, and MnO contents, which indicate they formed by partial melting of crustal rocks. In addition, the elemental ratios of these rhyolites and biotite granites are more consistent with a crustal than mantle source. For example, the Ba/Rb ratios (3.3–7.5; average = 4.3) are close to the crustal ratio (Ba/Rb = 6.7) of Rudnick and Fountain (1995) and are significantly lower than the mantle ratio

TABLE 4. ZIRCON Hf ISOTOPE DATA FOR THE PINGXIANG RHYOLITIC AND BIOTITE GRANITIC SAMPLES

Sample	T (Ma)	$^{176}Yb/^{177}Hf$	$^{176}Lu/^{177}Hf$	$^{176}Hf/^{177}Hf$	1Σ	$(^{176}Hf/^{177}Hf)i$	$\varepsilon_{Hf}(t)$	1Σ	$T_{(DM2)}$ (Ga)
19px-4-1	249	0.064960	0.001824	0.282440	0.000013	0.282432	–6.95	0.44	1.69
19px-4-2	248	0.037002	0.001091	0.282417	0.000011	0.282412	–7.69	0.39	1.74
19px-4-3	247	0.043660	0.001343	0.282414	0.000011	0.282408	–7.85	0.40	1.75
19px-4-4	249	0.033806	0.001028	0.282399	0.000012	0.282395	–8.28	0.41	1.78
19px-4-5	248	0.032796	0.001004	0.282414	0.000010	0.282410	–7.78	0.35	1.74
19px-4-6	249	0.024641	0.000794	0.282400	0.000011	0.282396	–8.22	0.38	1.77
19px-4-7	248	0.066239	0.002007	0.282407	0.000011	0.282397	–8.20	0.39	1.77
19px-4-8	250	0.035229	0.001119	0.282381	0.000011	0.282376	–8.92	0.40	1.82
19px-4-9	248	0.029766	0.000944	0.282390	0.000012	0.282385	–8.63	0.42	1.80
19px-4-10	247	0.037292	0.001140	0.282407	0.000012	0.282402	–8.07	0.43	1.76
19px-4-11	248	0.030847	0.000946	0.282401	0.000010	0.282397	–8.20	0.37	1.77
19px-4-12	249	0.053191	0.001660	0.282446	0.000012	0.282439	–6.71	0.43	1.68
19px-4-13	248	0.031078	0.000959	0.282389	0.000011	0.282384	–8.68	0.37	1.80
19px-4-14	249	0.041908	0.001262	0.282410	0.000010	0.282404	–7.96	0.37	1.76
19px-4-15	247	0.051658	0.001570	0.282407	0.000011	0.282400	–8.13	0.38	1.77
19px-4-16	250	0.057866	0.001776	0.282299	0.000009	0.282291	–11.92	0.33	2.00
19px-4-17	248	0.038670	0.001240	0.282286	0.000010	0.282280	–12.36	0.35	2.03
19px-4-18	249	0.018531	0.000607	0.282395	0.000012	0.282393	–8.34	0.42	1.78
19px-4-19	247	0.055142	0.001636	0.282418	0.000011	0.282411	–7.74	0.38	1.74
19px-4-20	248	0.020246	0.000633	0.282391	0.000010	0.282388	–8.52	0.36	1.79
19px-4-21	249	0.044716	0.001342	0.282355	0.000010	0.282348	–9.91	0.36	1.88
19px-4-22	248	0.028684	0.000876	0.282386	0.000011	0.282382	–8.76	0.39	1.80
19px-4-23	249	0.032724	0.000999	0.282409	0.000013	0.282404	–7.93	0.46	1.75
19px-4-24	249	0.021593	0.000673	0.282385	0.000012	0.282382	–8.72	0.41	1.80
19px-4-25	249	0.047178	0.001418	0.282226	0.000010	0.282219	–14.47	0.36	2.16
19px-4-26	248	0.029355	0.000941	0.282232	0.000019	0.282228	–14.19	0.66	2.15
19px-4-27	250	0.022909	0.000690	0.282403	0.000011	0.282400	–8.07	0.40	1.76
19px-4-28	250	0.036834	0.001051	0.282423	0.000011	0.282418	–7.42	0.37	1.72
19px-9-1	251	0.069912	0.001779	0.282380	0.000009	0.282372	–9.04	0.30	1.82
19px-9-2	252	0.063038	0.001573	0.282383	0.000011	0.282375	–8.88	0.37	1.82
19px-9-3	251	0.025180	0.000646	0.282296	0.000011	0.282293	–11.83	0.37	2.00
19px-9-4	252	0.063549	0.001573	0.282375	0.000009	0.282368	–9.17	0.30	1.83
19px-9-5	251	0.073201	0.001789	0.282451	0.000011	0.282443	–6.53	0.39	1.67
19px-9-6	252	0.054013	0.001336	0.282172	0.000009	0.282165	–16.31	0.32	2.28
19px-9-7	251	0.058027	0.001495	0.282357	0.000010	0.282350	–9.81	0.34	1.87
19px-9-8	250	0.049441	0.001259	0.282347	0.000010	0.282341	–10.14	0.34	1.89
19px-9-9	252	0.027178	0.000717	0.282069	0.000013	0.282065	–19.87	0.46	2.50
19px-9-10	251	0.097530	0.002463	0.282408	0.000011	0.282397	–8.16	0.39	1.77
19px-9-11	252	0.071642	0.001844	0.282366	0.000010	0.282357	–9.52	0.34	1.86
19px-9-12	251	0.109550	0.002820	0.282371	0.000010	0.282358	–9.53	0.35	1.86
19px-9-13	250	0.107674	0.002851	0.282371	0.000010	0.282358	–9.55	0.36	1.86
19px-9-14	252	0.049798	0.001324	0.282299	0.000009	0.282293	–11.83	0.31	2.00
19px-9-15	253	0.011629	0.000314	0.282112	0.000011	0.282111	–18.24	0.39	2.40
19px-9-16	250	0.042447	0.001116	0.282334	0.000009	0.282329	–10.60	0.31	1.92
19px-9-17	251	0.052078	0.001347	0.282257	0.000010	0.282250	–13.33	0.34	2.09
19px-9-18	250	0.055226	0.001441	0.282373	0.000009	0.282367	–9.25	0.31	1.84

(*continued*)

(Ba/Rb = 11; Hofmann and White, 1983). Moreover, the studied A_2-type rhyolites and biotite granites do not contain mafic microgranular enclaves and have negative $\varepsilon_{Nd}(t)$ (–11.5 to –9.7; T_{MD} = 1.8–2.0 Ga) and zircon $\varepsilon_{Hf}(t)$ values (–14.5 to –6.2; T_{MD} = 1.6–2.9 Ga) (Figs. 9 and 10), as well as high SiO_2 contents and low $Mg^{\#}$ values (Fig. 11A). These features indicate that the rhyolites and biotite granites were derived by partial melting of crustal materials rather than by differentiation of mantle-derived basaltic magmas or magma mixing between crust- and mantle-derived magmas. This inference is further supported by the low Cr (1.6–7.4 ppm) and Ni (0.2–6.0 ppm) contents of the studied rocks.

Several sources have been proposed to explain the formation of A-type granites with a crustal origin, including dry residual granulitic lower crust (Collins et al., 1982; Clemens et al., 1986), granulitic metasedimentary rocks (Huang et al., 2011), dehydrated charnockitic middle–lower crust (Zhao et al., 2008; Zhang et al., 2015), and hornblende- and biotite-bearing granitoids (Patiño Douce, 1997). Collins et al. (1982) and Clemens et al. (1986) proposed that A-type granites were derived by partial melting of dry residual granulitic lower crust from which a hydrous felsic melt phase had been extracted. However, Creaser et al. (1991) showed that a residual granulitic source is unlikely to generate A-type granitic melts, based on the major-element compositions of the likely partial melts and proposed source rocks. The studied A_2-type rhyolites and biotite granites are calc-alkaline with $(K_2O + Na_2O)/Al_2O_3$ ratios of 0.54–0.62, which are inconsistent with a metasedimentary source, because partial melting of crustal metasedimentary rocks typically produces low-melt alkali contents (Karsli et al., 2018). As such, dry residual granulitic lower-crustal and granulitic metasedimentary sources can both be precluded. In addition, the studied rhyolites and biotite granites have negative whole-rock $\varepsilon_{Nd}(t)$ and zircon $\varepsilon_{Hf}(t)$ values and old T_{DM2} ages, indicating the source was not juvenile middle–lower crust (Figs. 9A and 10).

A-type granites typically represent anhydrous high-temperature magmas (Clemens et al., 1986; Eby, 1992; Dall'Agnol et al., 2012; Wu et al., 2022), and their origins involve partial melting of crustal igneous rocks of tonalitic to granodioritic

TABLE 4. ZIRCON Hf ISOTOPE DATA FOR THE PINGXIANG RHYOLITIC AND BIOTITE GRANITIC SAMPLES (*continued*)

Sample	T (Ma)	$^{176}Yb/^{177}Hf$	$^{176}Lu/^{177}Hf$	$^{176}Hf/^{177}Hf$	1Σ	$(^{176}Hf/^{177}Hf)i$	$\varepsilon_{Hf}(t)$	1Σ	$T_{(DM2)}$ (Ga)
19px-9-19	252	0.049417	0.001363	0.282369	0.000010	0.282363	–9.34	0.35	1.84
19px-9-20	249	0.053339	0.001351	0.282384	0.000010	0.282377	–8.89	0.35	1.81
19px-9-21	250	0.052742	0.001374	0.282369	0.000009	0.282363	–9.36	0.31	1.84
19px-9-22	252	0.035099	0.000903	0.282344	0.000008	0.282340	–10.15	0.29	1.90
19px-9-23	251	0.052454	0.001384	0.282388	0.000009	0.282381	–8.71	0.31	1.80
19px-9-24	250	0.068897	0.001775	0.282361	0.000010	0.282353	–9.72	0.33	1.87
19px-9-25	251	0.045781	0.001211	0.282355	0.000008	0.282350	–9.81	0.28	1.87
19px-9-26	249	0.064662	0.001684	0.282354	0.000009	0.282346	–10.00	0.30	1.88
19px-9-27	251	0.059846	0.001551	0.282363	0.000010	0.282356	–9.59	0.34	1.86
19px-9-28	252	0.052175	0.001360	0.282334	0.000008	0.282327	–10.57	0.30	1.92
19px-9-29	251	0.048755	0.001258	0.282384	0.000010	0.282378	–8.79	0.34	1.81
19px-9-30	251	0.055467	0.001425	0.282355	0.000009	0.282348	–9.89	0.30	1.88
19px-9-31	251	0.043920	0.001175	0.282368	0.000011	0.282363	–9.36	0.37	1.85
19px-9-32	252	0.047025	0.001266	0.282289	0.000010	0.282283	–12.17	0.35	2.02
19px-9-33	251	0.057852	0.001502	0.282352	0.000009	0.282345	–9.97	0.30	1.88
19px-9-34	250	0.018715	0.000490	0.281873	0.000012	0.281871	–26.77	0.41	2.93
19px-9-35	252	0.033831	0.000887	0.282227	0.000009	0.282223	–14.28	0.30	2.15
19px-10-1	251	0.035892	0.001050	0.282406	0.000012	0.282401	–8.01	0.42	1.76
19px-10-2	251	0.013590	0.000409	0.281990	0.000018	0.281988	–22.60	0.65	2.67
19px-10-3	249	0.022234	0.000688	0.282408	0.000011	0.282405	–7.90	0.40	1.75
19px-10-4	251	0.028594	0.000881	0.282401	0.000010	0.282397	–8.15	0.36	1.77
19px-10-5	250	0.020992	0.000666	0.282386	0.000011	0.282383	–8.65	0.40	1.80
19px-10-6	250	0.028445	0.000901	0.282346	0.000011	0.282341	–10.14	0.39	1.89
19px-10-7	251	0.051742	0.001627	0.282352	0.000011	0.282344	–10.00	0.39	1.89
19px-10-8	251	0.023053	0.000720	0.282384	0.000011	0.282381	–8.72	0.37	1.81
19px-10-9	251	0.020058	0.000650	0.282386	0.000011	0.282383	–8.66	0.40	1.80
19px-10-10	251	0.024947	0.000784	0.282404	0.000012	0.282400	–8.04	0.42	1.76
19px-10-11	250	0.034996	0.001095	0.282275	0.000010	0.282270	–12.67	0.37	2.05
19px-10-12	251	0.027298	0.000737	0.282312	0.000011	0.282309	–11.27	0.39	1.96
19px-10-13	251	0.057445	0.001771	0.282332	0.000010	0.282324	–10.74	0.35	1.93
19px-10-14	250	0.020863	0.000659	0.282405	0.000010	0.282402	–7.98	0.35	1.76
19px-10-15	250	0.031214	0.000967	0.282315	0.000009	0.282311	–11.23	0.32	1.96
19px-10-16	250	0.020338	0.000633	0.282129	0.000010	0.282127	–17.73	0.35	2.37
19px-10-17	249	0.034292	0.001049	0.282454	0.000011	0.282449	–6.34	0.39	1.65
19px-10-18	250	0.021173	0.000692	0.282375	0.000013	0.282371	–9.08	0.45	1.83
19px-10-19	252	0.040719	0.001209	0.282420	0.000010	0.282414	–7.52	0.35	1.73
19px-10-20	251	0.019296	0.000612	0.282395	0.000011	0.282392	–8.33	0.38	1.78
19px-10-21	249	0.023957	0.000733	0.282391	0.000010	0.282388	–8.51	0.34	1.79
19px-10-22	250	0.078347	0.002341	0.282273	0.000011	0.282262	–12.95	0.39	2.07
19px-10-23	251	0.031102	0.000958	0.282355	0.000012	0.282350	–9.82	0.43	1.87
19px-10-24	251	0.037195	0.001098	0.282132	0.000009	0.282127	–17.69	0.33	2.37
19px-10-25	250	0.030404	0.000930	0.282429	0.000011	0.282424	–7.19	0.37	1.71
19px-10-26	250	0.028059	0.000853	0.282392	0.000011	0.282388	–8.50	0.39	1.79
19px-10-27	250	0.043621	0.001294	0.282233	0.000011	0.282227	–14.16	0.37	2.15
19px-10-28	250	0.027700	0.000823	0.282399	0.000012	0.282395	–8.24	0.41	1.77
19px-10-29	251	0.021809	0.000644	0.282384	0.000011	0.282381	–8.70	0.40	1.80
19px-10-30	252	0.035605	0.001043	0.282458	0.000012	0.282453	–6.13	0.44	1.64

composition (Creaser et al., 1991). Based on melting experiments of tonalite and granodiorite at 950 °C, Patiño Douce (1997) showed that the products of dehydration melting of hornblende- and biotite-bearing granitoids in the upper continental crust at low pressures ($P \leq 4$ kbar; depths ≤ 15 km) have geochemical characteristics similar to A_2-type granites (Figs. 11B and 11C). Moreover, plagioclase and orthopyroxene are the products of shallow ($P \leq 4$ kbar) dehydration melting of hornblende-bearing granitoids and become the dominant residual phases. Crystallization of plagioclase and orthopyroxene decreases the CaO and MgO contents of melts with decreasing pressure and explains the low CaO and MgO contents of A-type granites as well as their Eu and Sr depletions (Patiño Douce, 1997). The studied samples have low CaO (0.28–1.61 wt%) and MgO (0.40–0.84 wt%) contents and large negative Eu and Sr anomalies (Figs. 6B and 6D), which are consistent with a residual low-pressure mineral assemblage of plagioclase + orthopyroxene. Crystallization of plagioclase can also produce melts that are enriched in Ga relative to Al with high Ga/Al ratios (Patiño Douce, 1997). The studied granites have high Ga/Al ratios (10,000 × Ga/Al = 2.9–4.1). The $\varepsilon_{Nd}(t)$ values and $(Th/Nb)_N$ ratios of our samples are similar to those of granites formed by partial melting of felsic crustal rocks but different from those of granites and rhyolites formed by partial melting of charnockites or juvenile middle to lower crust (Fig. 9B). Furthermore, the magma underwent variable degrees of fractional crystallization and finally formed the biotite granite and rhyolite melt. Therefore, we propose that the A_2-type rhyolites and biotite granites in the Pingxiang area might have been generated by partial melting of felsic crustal rocks at low pressures of ~4 kbar (Figs. 11B and 11C) and high temperatures of ~860 °C (Fig. 11D), and then the magma underwent fractional crystallization that formed the biotite granite and equivalent rhyolite melt.

6.2. Tectonic Implications and Geodynamic Model

The tectonic setting of the studied rhyolites and granites can be evaluated with a series of tectonic

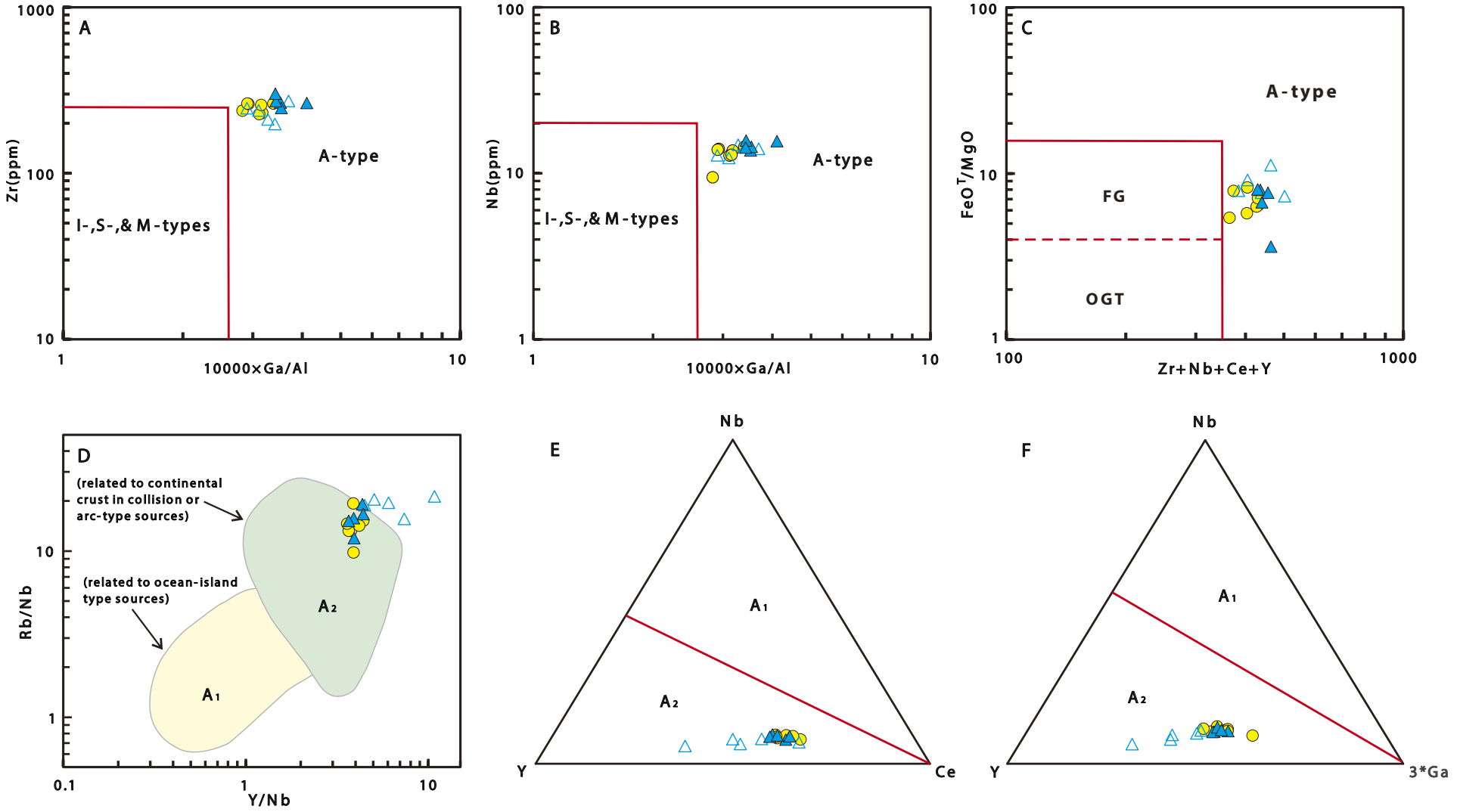

Figure 7. Plots of (A) Zr versus 10,000 × Ga/Al; (B) Nb versus 10,000 × Ga/Al; (C) FeO^T/MgO versus (Zr + Nb + Ce + Y) after Whalen et al. (1987); (D) Rb/Nb versus Y/Nb; (E) Nb-Y-Ce; and (F) Nb-Y-3 × Ga after Eby (1992). The symbols are as in Figure 5. FG—fractionated felsic granites; OGT—unfractionated I-, S-, and M-type granites; A_1—anorogenic A-type granites; A_2—post-collisional A-type granites.

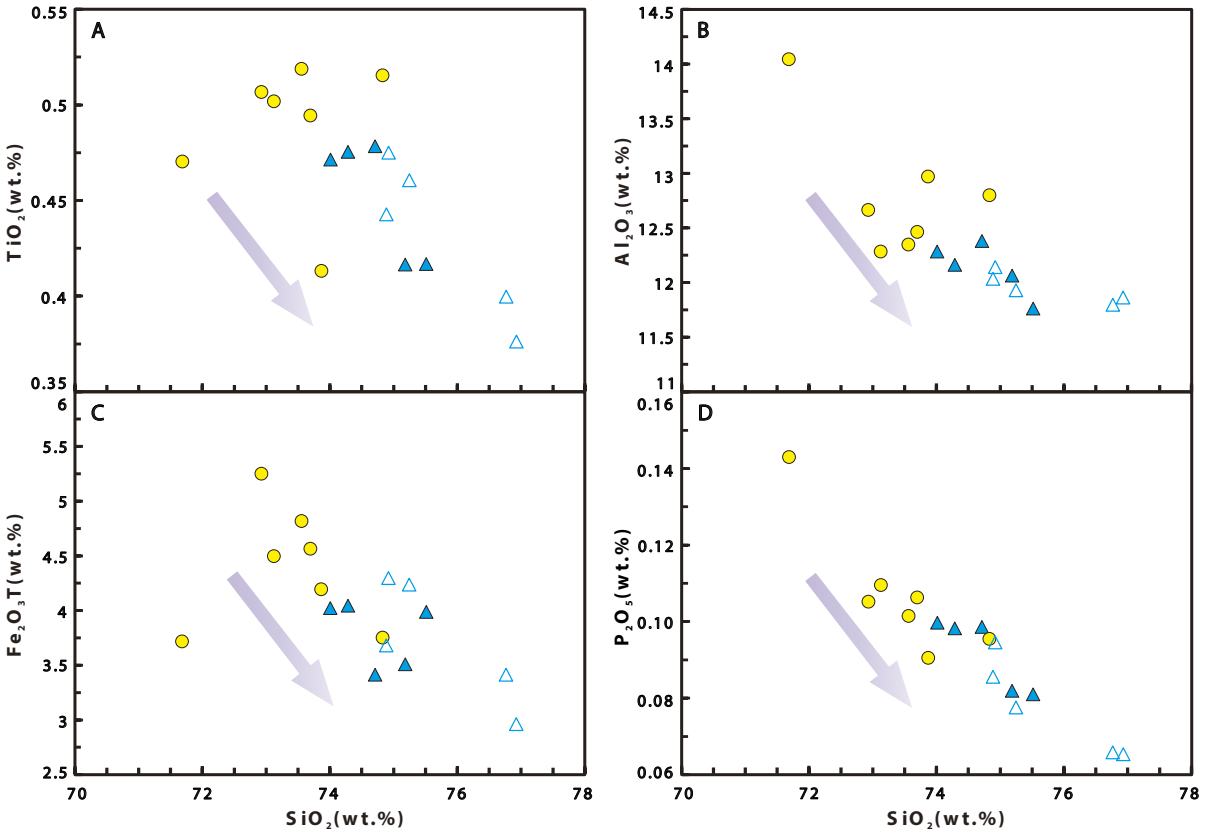

Figure 8. Harker diagrams for selected major elements.

discrimination diagrams (Fig. 12). On the Rb/30-Hf-Ta × 3 and Nb versus SiO_2 tectonic classification diagrams (Figs. 12A and 12B), all the samples plot in the volcanic arc granite field. On Al_2O_3/SiO_2 versus Fe_2O_3 + MgO and Th/Ta versus Yb diagrams (Figs. 12C and 12D), the studied rocks plot in the active continental margin igneous rock field. Zircon trace-element contents can be used to constrain the tectonic setting of the studied rhyolitic and biotite granitic magmas (Yang et al., 2012). Most zircon grains in the rhyolites and biotite granites have Nb/Hf, Th/U, Th/Nb, Hf/Th, Nb/Yb, and U/Yb ratios similar to those of zircons from arc-related settings and plot in the arc-related (i.e., orogenic) and continental arc fields in plots of Nb/Hf versus Th/U, Hf/Th versus Th/Nb (Figs. 13A and 13B), and $\log_{10}$(U/Yb) versus $\log_{10}$(Nb/Yb) (Fig. 13C). Thus, these zircon grains have a trace-element geochemistry similar to that of zircons formed in an arc setting (Peng et al., 2008; Yang et al., 2012; Grimes et al., 2015).

It has been suggested that the Permian–Triassic igneous rocks in the southwestern SCB are related to either Paleo-Tethys subduction and closure (Jiao et al., 2015; Li et al., 2016; Xu et al., 2018; Wang et al., 2020; Gan et al., 2021) or Paleo-Pacific subduction (Li et al., 2006, 2012b; Li and Li, 2007). The Paleozoic–Mesozoic ophiolites, high-pressure and low-temperature metamorphic rocks, and arc igneous rocks in the Ailaoshan–Song Ma suture zone are indicative of subduction in the Paleo-Tethys Ocean (Xu et al., 2007; Zi et al., 2012b; Hou et al., 2017; Liu et al., 2018). The late Permian to early Triassic tholeiites in the Jianshui, Napo, and Pingxiang areas of the southwestern Youjiang Basin, as well as the brachiopods and other fossils in siliceous shales and chert interbeds, suggest that early Mesozoic magmatism in the Pingxiang region was related to subduction and closure of the eastern Paleo-Tethys Ocean (Dong and Zhu, 1999; Wu et al., 2000, 2002). The Youjiang Basin is close to the Ailaoshan–Song Ma suture zone between the SCB and Indochina

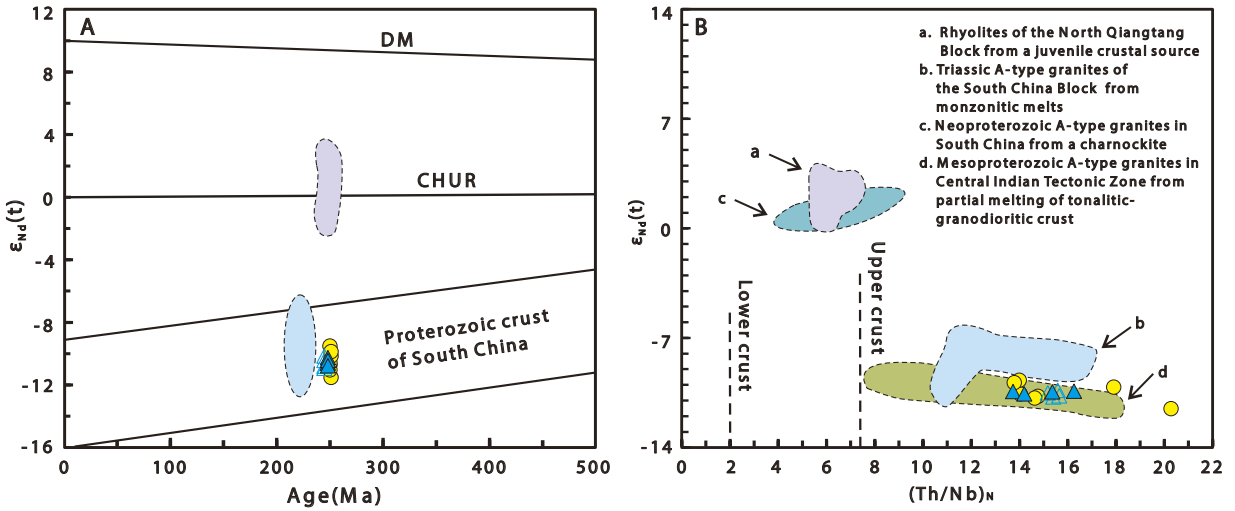

Figure 9. Plots of (A) $\varepsilon_{Nd}(t)$ versus age (after Shen et al., 1993) and (B) $\varepsilon_{Nd}(t)$ versus $(Th/Nb)_N$ (after Pham et al., 2020). The symbols are as in Figure 5, and the data sources are as in Table 3. CHUR—chondritic uniform reservoir; DM—depleted mantle. Data sources: North Qiangtang Block A-type rhyolite data are from Zhang et al. (2020); Triassic A-type granite data for the South China Block (SCB) are from Xia and Xu (2020); Neoproterozoic A-type granite data for South China are from Zhao et al. (2008); Indian tectonic zone A-type granite data are from Yadav et al. (2020).

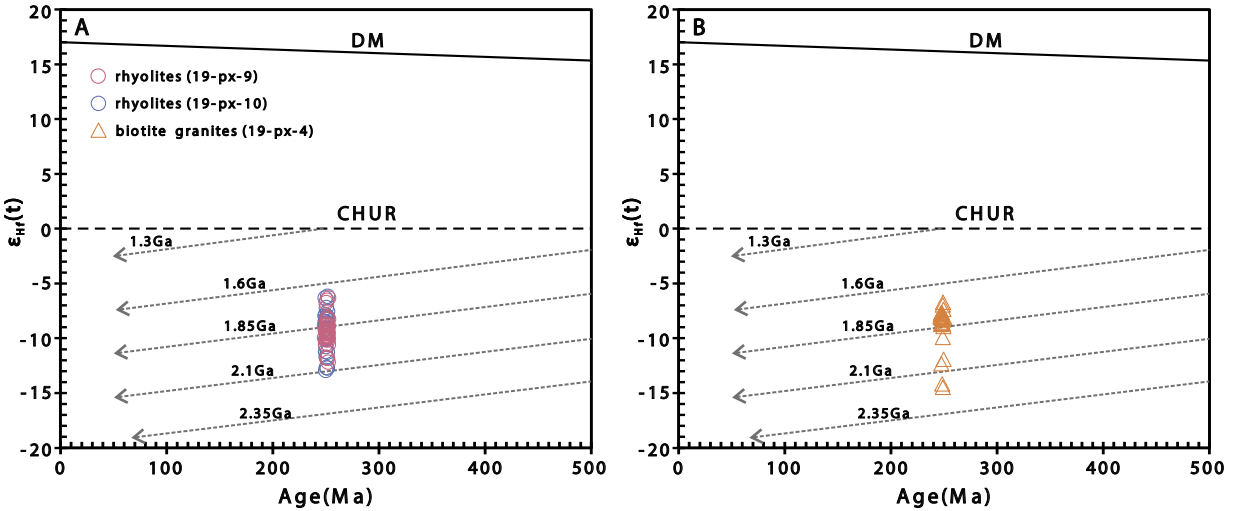

Figure 10. Plots of zircon $\varepsilon_{Hf}(t)$ values versus U-Pb ages for the (A) rhyolites and (B) biotite granites (after Wang et al., 2020). Data sources are as in Table 4. CHUR—chondritic uniform reservoir; DM—depleted mantle.

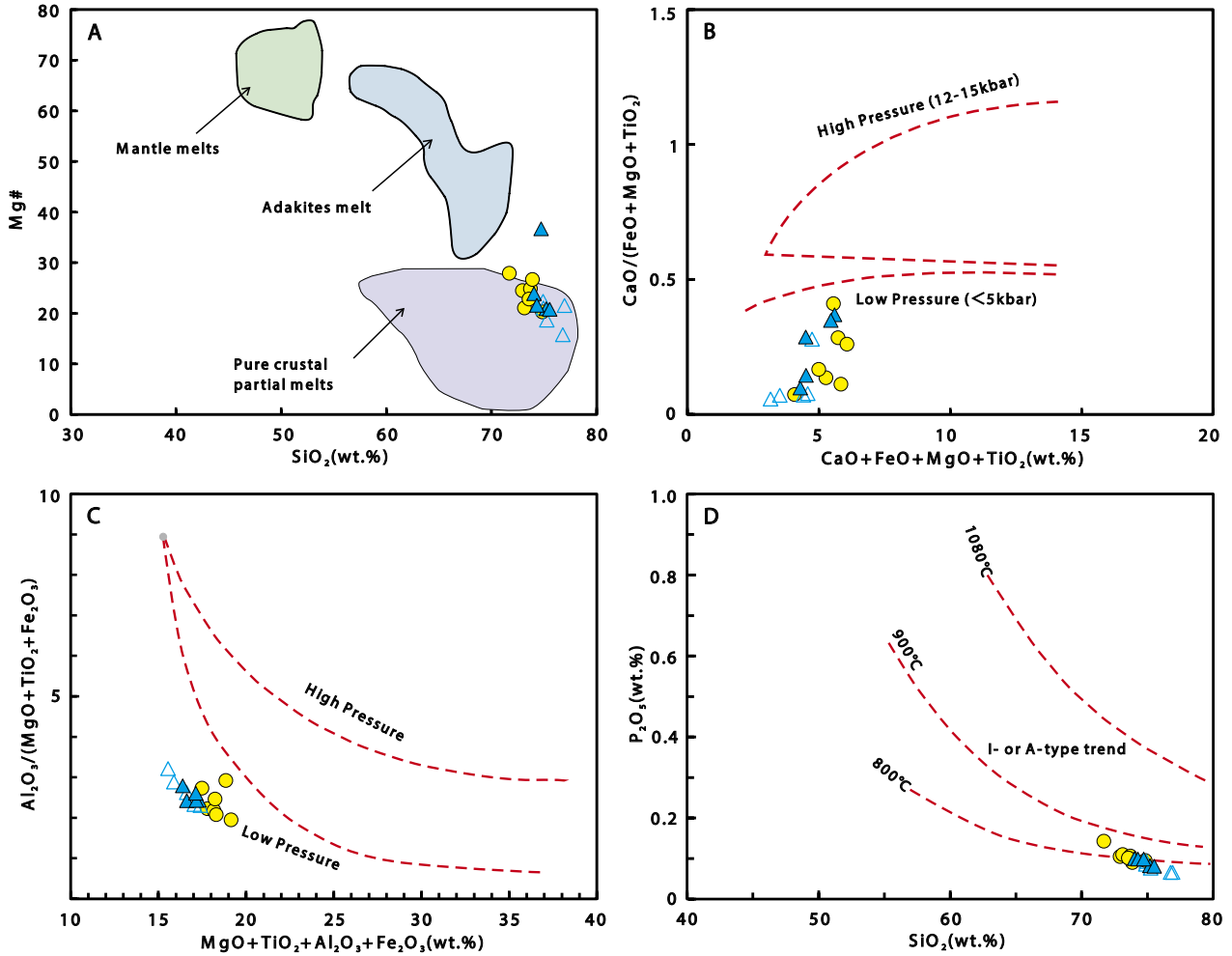

Figure 11. (A) Mg# versus SiO_2 diagram (after Zhao et al., 2019). (B and C) Compositional diagrams for the rhyolites and biotite granites in the Pingxiang area. The dashed lines are reaction curves. The area between the high-pressure (12–15 kbar) and low-pressure (≤5 kbar) curves is the range of depths at which mantle-crust interactions occur (Patiño Douce, 1999). (D) P_2O_5 versus SiO_2 diagram (after Xia and Xu, 2020). The symbols are as in Figure 5.

Block (Figs. 1 and 2A) but was far from the Pacific Ocean trench during the Triassic (Gan et al., 2021). The late Paleozoic to Triassic detrital zircons and volcanic lithic fragments in the Youjiang Basin indicate a detrital input from an Indosinian orogenic belt (Yang et al., 2012; Hu et al., 2015a, 2015b); this input was triggered by subduction-collision in the Paleo-Tethys Ocean (Cai et al., 2014). Based on the distribution of known paleo-subduction zones in the surrounding regions and the regional sedimentary and igneous rock associations, we conclude that formation of rhyolites and biotite granites in the Pingxiang region was linked to Paleo-Tethys rather than Paleo-Pacific subduction.

Many authors agree that the tectonic evolution of the Paleo-Tethys Ocean included subduction of an oceanic plate followed by continental collision, crustal thickening, and extensional tectonics (Qin et al., 2013; Yang et al., 2014; Li et al., 2019). The Permian–Triassic Paleo-Tethys evolution can be constrained from magmatism of this age. Late

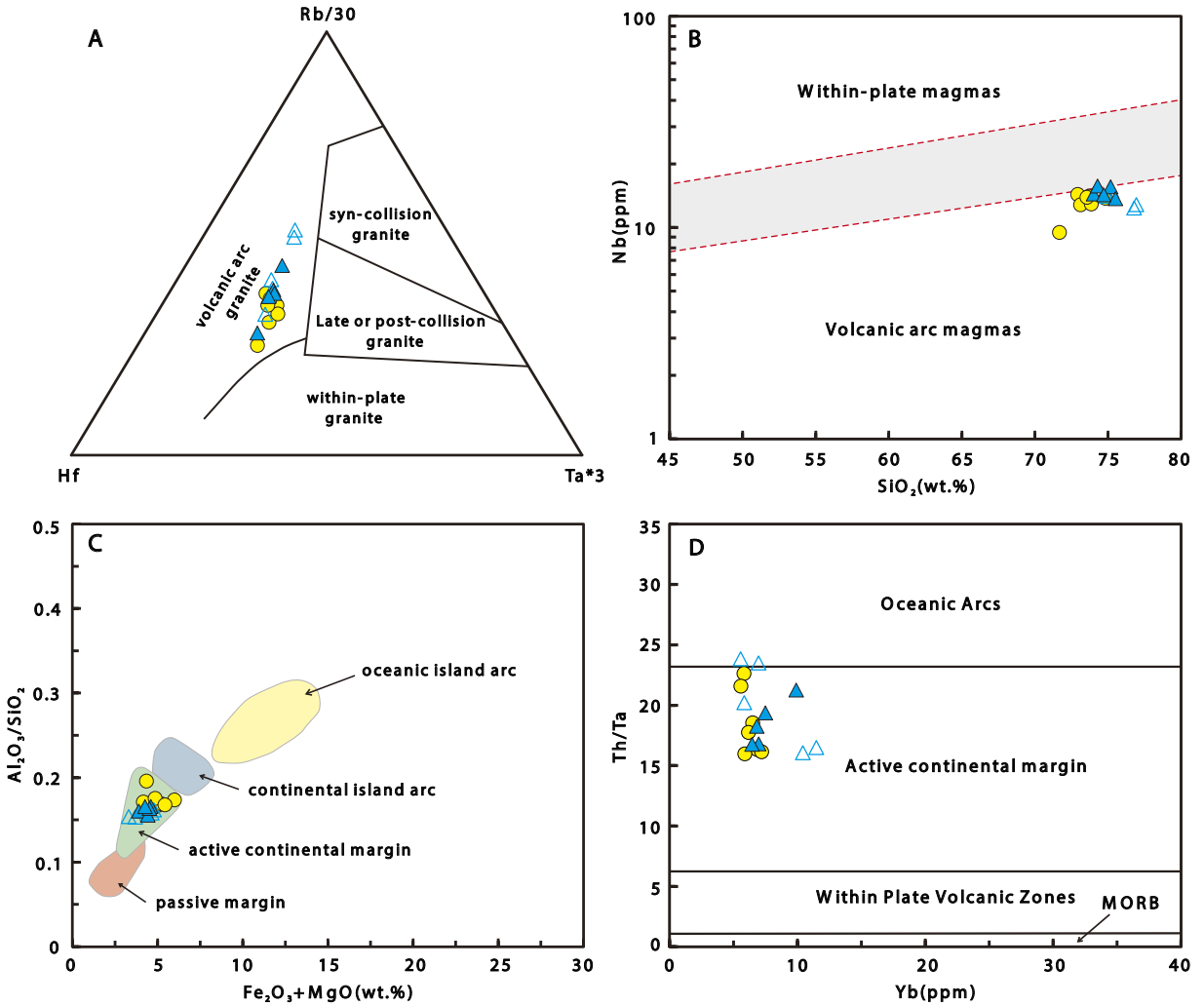

Figure 12. Tectonic discrimination diagrams for the rhyolites and biotite granites: (A) Rb/30-Hf-Ta × 3 (Harris et al., 1986); (B) Nb versus SiO_2 (Pearce and Gale, 1977); (C) Al_2O_3/SiO_2 versus Fe_2O_3+ MgO (Bhatia, 1983); and (D) Th/Ta versus Yb (Schandl and Gorton, 2002) diagrams. The symbols are as in Figure 5.

Permian–early Triassic arc granites and volcanic rocks are widespread in southeastern Guangxi and Hainan provinces and are considered to have formed due to northward subduction in the eastern Paleo-Tethys (Jiao et al., 2015; Li et al., 2016; Xu et al., 2018; Wang et al., 2020). The middle–late Triassic volcanic rocks from the nearby Sanjiang orogenic belt record the transition from a continental arc to a syn-collisional volcanic setting (Fan et al., 2014; Zhang et al., 2017; Yang et al., 2020). This was followed by late Triassic mafic and silicic volcanism, with little or no intermediate volcanism. This bimodal volcanism is typical of an extensional tectonic setting (Brewer et al., 2004; Chen et al., 2021). The composite Lincang batholith records the evolution of the Paleo-Tethys Ocean, including subduction in the late Permian–early Triassic, followed by the syn-collisional stage in the middle Triassic and post-collisional stage in

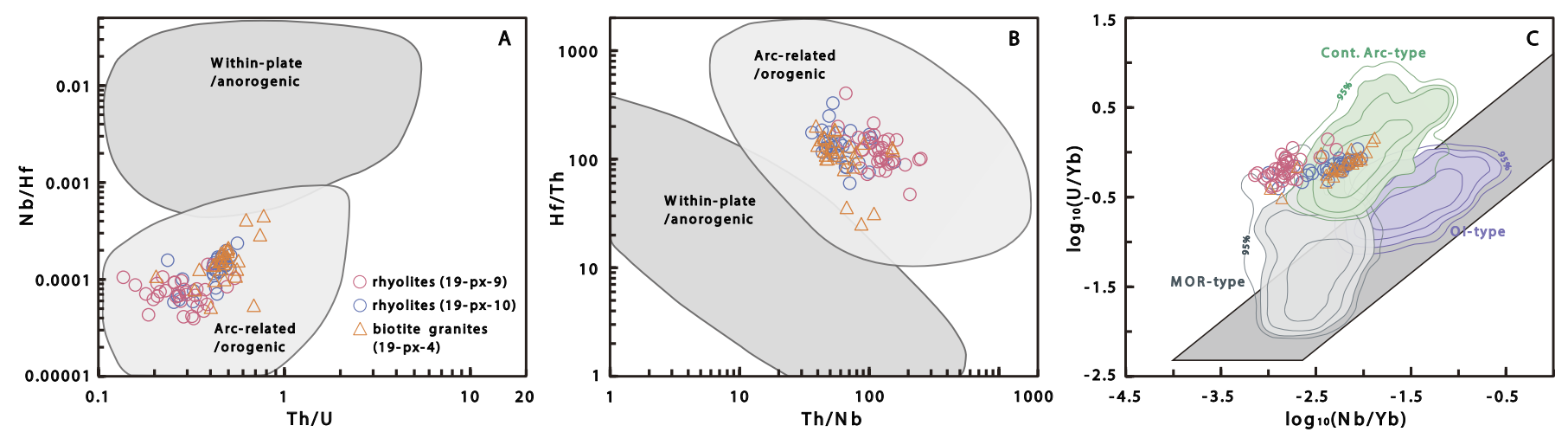

Figure 13. (A and B) Plots of zircon Nb/Hf versus Th/U and Hf/Th versus Th/Nb ratios (after Yang et al., 2012). On the two discrimination diagrams, the zircons from within-plate and anorogenic settings form two distinct clusters. (C) Zircon log_{10}(U/Yb) versus log_{10}(Nb/Yb) density distribution plot (after Grimes et al., 2015). The shaded fields are overlapping two-dimensional kernel density distributions for compiled data sets of mid-ocean ridge (MOR-type), plume-influenced Iceland and Hawaii (ocean island [OI]-type), and continental arc (Cont. arc-type) zircons. The contours are for the 50%, 80%, 90%, and 95% confidence levels and represent the proportion of data inside each contour.

the late Triassic (Peng et al., 2013; Deng et al., 2018). Chen et al. (2002, 2008) proposed that Jurassic granites, mafic igneous rocks, and bimodal volcanic rocks in the Nanling region of South China were the products of post-collisional extension of the Indosinian orogeny related to large-scale Tethys tectonism. As such, in the Permian–Triassic Paleo-Tethys Ocean, oceanic subduction occurred in the late Permian–early Triassic, the transition from subduction to syn-collision occurred during the middle–late Triassic, and post-collision and crustal extension occurred in or after the late Triassic.

The studied A_2-type rhyolites yielded weighted-mean $^{206}Pb/^{238}U$ ages of 250 ± 1 Ma, revealing that rhyolite eruption occurred in the early Triassic. The new zircon U-Pb age data for the A_2-type biotite granites from the Fuboshan pluton show they were emplaced at 249 ± 1 Ma in the early Triassic. Therefore, the rhyolites and biotite granites in the Pingxiang area were coeval and formed during subduction in the Paleo-Tethys Ocean but before its final closure during the middle Triassic.

The Pingxiang area is located at the southwestern margin of the Youjiang Basin (Fig. 1). Qiu et al. (2017) suggested that the Youjiang Basin was in an arc-related setting in the early Mesozoic, based on a study of clastic sedimentary rocks, whereas continent-continent collisional and post-collisional extensional settings did not exist based on the following geological evidence: (1) from the middle Devonian to early Triassic, complex platform and deep-sea sedimentation occurred in the Youjiang Basin (Cai and Zhang, 2009); (2) crustal deformation in the Youjiang Basin formed a thin-skinned, fold-and-thrust system during collision between the SCB and Indochina Block and the coeval Triassic oceanic subduction (Wang et al., 2020); (3) a detailed investigation of the Lopingian (upper Permian) to middle Triassic sequences of the Youjiang Basin constrained the patterns of basin fill, differential tectonic subsidence, and very high subsidence rates along regional faults, which are indicative of an extensional or transtensional continental back-arc setting prior to the middle Triassic (Duan et al., 2020); and (4) at the southern margin of the Youjiang Basin, basalts and andesites formed from 256 Ma to 241 Ma exhibit subduction-related arc-like features (Qin et al., 2011, 2012; Li et al., 2019; Wang et al., 2020). These lines of evidence demonstrate that the Pingxiang region was in a subduction rather than a continent-continent collisional or post-collisional extensional setting during the early Triassic.

With regards to the subduction polarity, several studies have suggested that the Ailaoshan–Song Ma suture records westward subduction beneath the Indochina Block during the Permian–Triassic (Wei and Shen, 1997; Liu et al., 2011, 2012; Halpin et al., 2016). However, east-dipping subduction beneath the SCB has also been proposed, based on Permian–Triassic sedimentary and paleontological evidence (e.g., the radiolarian assemblage in Qinfang Basin) in the southwest SCB (Hou et al., 2017; Ke et al., 2018; Xu et al., 2019) and arc-type igneous rocks (Fan et al., 2010; Qin et al., 2011, 2012; Wang et al., 2013; Zhang et al., 2014; Wu et al., 2015). For example, the middle Triassic silicic (e.g., dacite and rhyolite) and mafic (e.g., basalt) volcanic rocks in southwest Guangxi Province are geochemically similar to typical subduction-related arc volcanic rocks (Qin et al., 2011, 2012). Regarding the northern Song Ma suture zone, Lepvrier et al. (2004) and Zhang et al. (2014) proposed that eastwards

(based on the present-day position but originally northwards) oblique subduction occurred in the Paleo-Tethys beneath the SCB during 254–240 Ma, based on structural and geochronological studies of metamorphic rocks in the Indochina Block. Previous studies of early–middle Triassic volcanic (basaltic andesite)-sedimentary (carbonate-rich conglomerate, pebbly coarse sandstone, and calcareous sandstone) rock assemblages in the Napo-Funing area around Youjiang Basin indicate that the basin was in an active continental margin setting during the Permian–Triassic (Xiang et al., 2021). Therefore, we prefer the hypothesis whereby the middle Triassic Paleo-Tethys Ocean was experiencing bidirectional subduction to both the west and east beneath the Indochina Block and SCB, respectively (Xu et al., 2020). This subduction model can explain the early Triassic A_2-type granitic and rhyolitic magmatism in the Pingxiang area. The studied samples have arc-like geochemical features similar to those of A_2-type rhyolites (Eby, 1992; Eby et al., 1995) and I-type granites that form in extensional settings at convergent margins (e.g., the Simao terrane, Wusu arc, and Youjiang Basin; Figs. 5 and 6; He et al., 2018; Yang et al., 2018; Gan et al., 2021), and thus we suggest they formed in a similar extensional setting.

Data from previous studies and our new data for rhyolites and biotite granites in the Pingxiang area suggest the studied rocks represent magmas generated by subduction in the Paleo-Tethys Ocean along the Ailaoshan–Song Ma suture zone prior to its final closure, which was associated with slab roll-back during subduction in the Paleo-Tethys Ocean. Slab roll-back tends to occur when relatively old oceanic crust is being subducted (Niu, 2014), and this may induce upwelling of asthenosphere to compensate for the volume loss in the mantle wedge (Uyeda and Kanamori, 1979). This upwelling results in trenchward migration of arc magmatism and lithospheric extension and crustal melting in the rear-arc regions (Nakakuki and Mura, 2013; Liu et al., 2017; Collins et al., 2019). For example, the A-type granitoids in the Lachlan orogen, southeastern Australia, have been linked to extension associated with episodic slab roll-back (Collins et al., 2019). Arc magmatism at the southwestern margin of the Youjiang Basin during the early Triassic migrated from southeast to southwest, and arc magmatism occurred mainly from 265 Ma to 208 Ma (Qin et al., 2011; Gao et al., 2017; Li et al., 2019; Wei et al., 2020); the arc magmatism exhibits a general younging trend to the southwest. This trend is consistent with roll-back of the subducting Paleo-Tethys oceanic slab. Therefore, a slab roll-back model is proposed to explain the magmatism in the Pingxiang area (Fig. 14). During the early Triassic, the Paleo-Tethys oceanic slab was subducted

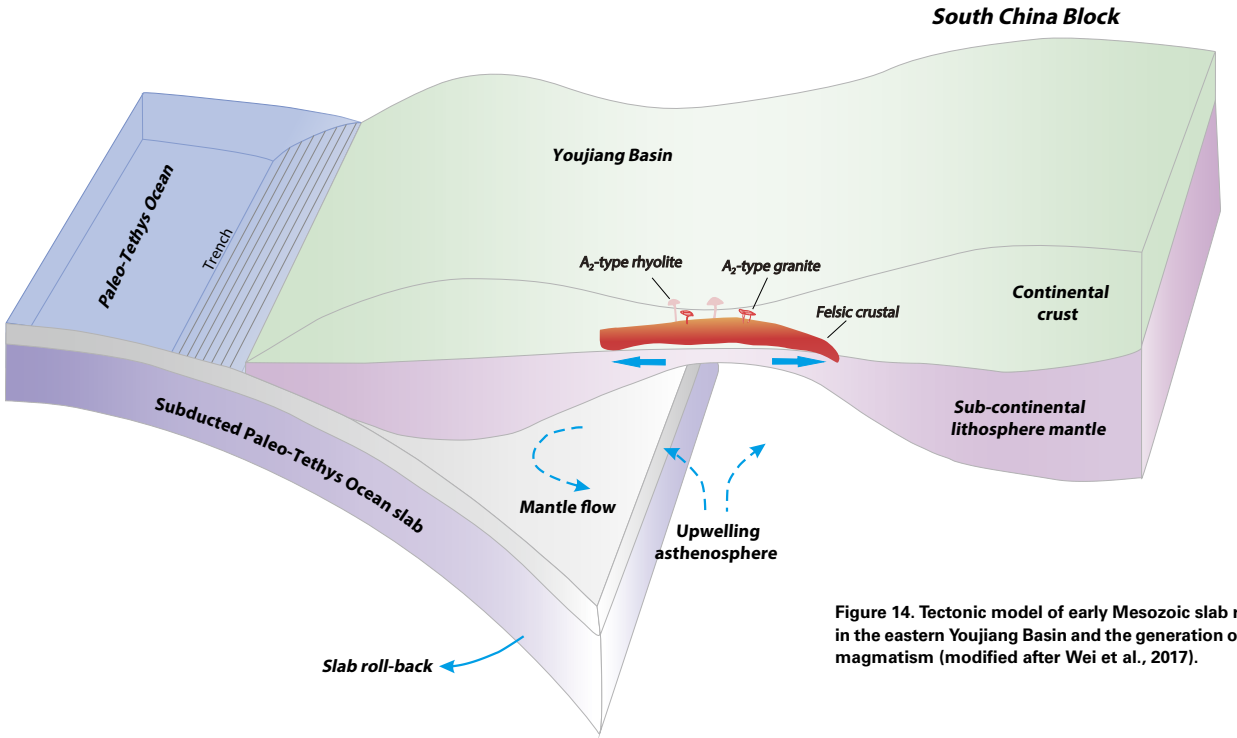

Figure 14. Tectonic model of early Mesozoic slab roll-back in the eastern Youjiang Basin and the generation of related magmatism (modified after Wei et al., 2017).

beneath the SCB, and slab roll-back caused asthenospheric upwelling, which led to the crust and mantle beneath the region becoming progressively thinner. The asthenospheric upwelling heated the subcontinental lithospheric mantle, triggered the partial melting of felsic crustal rocks, and generated the A_2-type rhyolitic and biotite granitic melts that were erupted and intruded in the Youjiang extensional setting.

7. CONCLUSIONS

Zircon U-Pb age and Hf isotope and whole-rock geochemical and Nd isotope data for newly discovered A_2-type rhyolites and biotite granites in the Pingxiang area of western Guangxi Province, southwest China, show that:

(1) The A_2-type rhyolites and biotite granites formed in the early Triassic (ca. 251–249 Ma).
(2) The rhyolites and biotite granites formed by partial melting of felsic crustal rocks at low pressures and high temperatures.
(3) The rhyolites and biotite granites likely formed in an extensional setting induced by slab roll-back during subduction of eastern Paleo-Tethys oceanic lithosphere during the early Triassic.

ACKNOWLEDGMENTS

We thank the GSA editor for handling and three anonymous reviewers for constructive criticism and suggestions that significantly improved this paper. This research was supported by the National Natural Science Foundation of China (grants 92055208 and 42203051), the Guangxi Natural Science Foundation of China (grant 2022GXNSFBA035538), the Guangxi Science Innovation Base Construction Foundation (grant GuikeZY21195031), the Guangxi Natural Science Foundation of China for Young Scholars (grant 2022GXNSFBA035538), and the Fifth Bagui Scholar Innovation Project of Guangxi Province (to Xu Jifeng). This is a contribution to the Guangxi Key Mineral Resources Deep Exploration Talent Highland.

REFERENCES CITED

Bhatia, M., 1983, Plate tectonics and geochemical composition of sandstones: The Journal of Geology, v. 91, no. 6, p. 611–627, https://doi.org/10.1086/628815.

Blichert-Toft, J., and Albarède, F., 1997, The Lu-Hf isotope geochemistry of chondrites and the evolution of the mantle-crust system: Earth and Planetary Science Letters, v. 148, no. 1–2, p. 243–258, https://doi.org/10.1016/S0012-821X(97)00040-X.

Bonin, B., 2007, A-type granites and related rocks: Evolution of a concept, problems and prospects: Lithos, v. 97, no. 1–2, p. 1–29, https://doi.org/10.1016/j.lithos.2006.12.007.

Boynton, W.V., 1984, Geochemistry of the rare earth elements: Meteorite studies, *in* Henderson, P., ed., Rare Earth Elements Geochemistry: New York, Elsevier, v. 2, http://doi.org/10.1016/B978-0-444-42148-7.50008-3.

Brewer, T.S., Åhäll, K.I., Menuge, J.F., Storey, C.D., and Parrish, R.R., 2004, Mesoproterozoic bimodal volcanism in SW Norway, evidence for recurring pre-Sveconorwegian continental margin tectonism: Precambrian Research, v. 134, no. 3–4, p. 249–273, https://doi.org/10.1016/j.precamres.2004.06.003.

Cai, J., Tan, X., and Wu, Y., 2014, Magnetic fabric and paleomagnetism of the Middle Triassic siliciclastic rocks from the Nanpanjiang Basin, South China: Implications for sediment provenance and tectonic process: Journal of Asian Earth Sciences, v. 80, p. 134–147, https://doi.org/10.1016/j.jseaes.2013.10.033.

Cai, J.X., and Zhang, K.J., 2009, A new model for the Indochina and South China collision during the Late Permian to the Middle Triassic: Tectonophysics, v. 467, no. 1–4, p. 35–43, https://doi.org/10.1016/j.tecto.2008.12.003.

Cai, J.X., Tang, X.C., Wei, Q.G., and Li, B., 2008, Comment on *Was the Indosinian orogeny a Triassic mountain building or a thermotectonic reactivation event?* by A. Carter and P.D. Clift: Comptes Rendus Geoscience, v. 340, no. 12, p. 893–895, https://doi.org/10.1016/j.crte.2008.09.004.

Cao, W., Yan, D.P., Qiu, L., Zhang, Y., and Qiu, J., 2015, Structural style and metamorphic conditions of the Jinshajiang metamorphic belt: Nature of the Paleo-Jinshajiang orogenic belt in the eastern Tibetan Plateau: Journal of Asian Earth Sciences, v. 113, p. 748–765, https://doi.org/10.1016/j.jseaes.2015.09.003.

Chen, C.H., Lee, C.Y., and Shinjo, R., 2008, Was there Jurassic Paleo-Pacific subduction in South China?: Constraints from $^{40}Ar/^{39}Ar$ dating, elemental and Sr-Nd-Pb isotopic geochemistry of the Mesozoic basalts: Lithos, v. 106, no. 1–2, p. 83–92, https://doi.org/10.1016/j.lithos.2008.06.009.

Chen, P.R., Hua, R.M., Zhang, B.T., Lu, J.J., and Fan, C.F., 2002, Early Yanshanian post-orogenic granitoids in the Nanling region: Petrological constraints and geodynamic settings: Science in China Series D: Earth Sciences, v. 45, p. 755–768, https://doi.org/10.1007/BF02878432.

Chen, Q., Wang, C., Bagas, L., Du, B., Shi, K., Yang, L., Zhu, J., and Duan, H., 2021, Petrogenesis of the Late Triassic Biluoxueshan granitic pluton, SW China: Implications for the tectonic evolution of the Paleo-Tethys Sanjiang Orogen: Journal of Asian Earth Sciences, v. 211, https://doi.org/10.1016/j.jseaes.2021.104700.

Clemens, J.D., Holloway, J.R., and White, A.J.R., 1986, Origin of an A-type granite; experimental constraints: The American Mineralogist, v. 71, no. 3–4, p. 317–324.

Collins, W., Huang, H.Q., Bowden, P., and Kemp, A., 2019, Repeated S- I- A-type granite trilogy in the Lachlan Orogen, and geochemical contrasts with A-type granites in Nigeria: Implications for petrogenesis and tectonic discrimination, *in* Janoušek, V., ed., Post-Archean Granitic Rocks: Petrogenetic Processes and Tectonic Environments: Geological Society, London, Special Publication 491, p. 53–76, https://doi.org/10.1144/SP491-2018-159.

Collins, W.J., Beams, S.D., White, A.J.R., and Chappell, B.W., 1982, Nature and origin of A-type granites with particular reference to southeastern Australia: Contributions to Mineralogy and Petrology, v. 80, no. 2, p. 189–200, https://doi.org/10.1007/BF00374895.

Creaser, R., Price, R., and Wormald, R., 1991, A-type granites revisited: Assessment of a residual-source model: Geology, v. 19, no. 2, p. 163–166, https://doi.org/10.1130/0091-7613(1991)019<0163:ATGRAO>2.3.CO;2.

Dall'Agnol, R., and de Oliveira, D.C., 2007, Oxidized, magnetite-series, rapakivi-type granites of Carajás, Brazil: Implications for classification and petrogenesis of A-type granites: Lithos, v. 93, no. 3–4, p. 215–233, https://doi.org/10.1016/j.lithos.2006.03.065.

Dall'Agnol, R., Frost, C.D., and Rämö, O.T., 2012, IGCP Project 510 "A-type Granites and Related Rocks through Time": Project vita, results, and contribution to granite research: Lithos, v. 151, p. 1–16, https://doi.org/10.1016/j.lithos.2012.08.003.

Deng, J., Wang, C., Zi, J.W., Xia, R., and Li, Q., 2018, Constraining subduction-collision processes of the Paleo-Tethys along the Changning-Menglian Suture: New zircon U-Pb ages and Sr-Nd-Pb-Hf-O isotopes of the Lincang Batholith: Gondwana Research, v. 62, p. 75–92, https://doi.org/10.1016/j.gr.2017.10.008.

Dong, Y.P., and Zhu, B.Q., 1999, Jianshui island-arc pillow basalts in southeastern Yunnan and their constraints on Paleotethys in South China: Scientific Bulletin of China, v. 44, no. 21, p. 2323–2328 [in Chinese with English abstract].

Du, Y.S., Huang, H., Yang, J.H., Huang, H.W., Tao, P., Huang, Z.Q., Hu, L.S., and Xie, C.X., 2013, The basin translation from Late Paleozoic to Triassic of the Youjiang Basin and its tectonic signification: Geological Review (Dizhi Lunping), v. 59, no. 01, p. 1–11 [in Chinese with English abstract].

Duan, L., Meng, Q.R., Wu, G.L., Yang, Z., Wang, J., and Zhan, R., 2020, Nanpanjiang basin: A window on the tectonic development of south China during Triassic assembly of the southeastern and eastern Asia: Gondwana Research, v. 78, p. 189–209, https://doi.org/10.1016/j.gr.2019.08.009.

Eby, G.N., 1990, The A-type granitoids: A review of their occurrence and chemical characteristics and speculations on their petrogenesis: Lithos, v. 26, no. 1–2, p. 115–134, https://doi.org/10.1016/0024-4937(90)90043-Z.

Eby, G.N., 1992, Chemical subdivision of the A-type granitoids: Petrogenetic and tectonic implications: Geology, v. 20, no. 7, p. 641–644, https://doi.org/10.1130/0091-7613(1992)020<0641:CSOTAT>2.3.CO;2.

Eby, G.N., Roden-Tice, M., Krueger, H.L., Ewing, W., Faxon, E.H., and Woolley, A.R., 1995, Geochronology and cooling history of the northern part of the Chilwa Alkaline Province, Malawi: Journal of African Earth Sciences, v. 20, no. 3–4, p. 275–288, https://doi.org/10.1016/0899-5362(95)00054-W.

Fan, J.W., Yang, T.N., Liang, M.J., and Shi, P.L., 2014, LA-ICP-MS zircon U-Pb geochronology and geochemistry of volcanic rocks on the western margin of Lanping Basin in western Yunnan and their tectonic implications: Acta Petrologica et Mineralogica, v. 33, no. 3, p. 471–490 [in Chinese with English abstract].

Fan, W., Wang, Y., Zhang, A., Zhang, F., and Zhang, Y., 2010, Permian arc—back-arc basin development along the Ailaoshan

tectonic zone: Geochemical, isotopic and geochronological evidence from the Mojiang volcanic rocks, Southwest China: Lithos, v. 119, no. 3–4, p. 553–568, https://doi.org/10.1016/j.lithos.2010.08.010.

Fromaget, J., 1941, L'Indochine francaise, sa structure geologique, ses roches, ses mines et leurs relations possibles avec la tectonique: Hanoi, Impr. d'Extreme-Orient, Bulletin du service geologique de l'Indochine, v. 26, https://nla.gov.au/nla.cat-vn821618.

Frost, B.R., Barnes, C.G., Collins, W.J., Arculus, R.J., Ellis, D.J., and Frost, C.D., 2001, A Geochemical Classification for Granitic Rocks: Journal of Petrology, v. 42, no. 11, p. 2033–2048, https://doi.org/10.1093/petrology/42.11.2033.

Gan, C., Wang, Y., Zhang, Y., Xin, Q., and Zhang, A., 2021, The assembly of the South China and Indochina blocks: Constraints from the Triassic felsic volcanics in the Youjiang Basin: Geological Society of America Bulletin, v. 133, no. 9–10, p. 2097–2112, https://doi.org/10.1130/B35816.1.

Gao, P., Zheng, Y.F., and Zhao, Z.F., 2017, Triassic granites in South China: A geochemical perspective on their characteristics, petrogenesis, and tectonic significance: Earth-Science Reviews, v. 173, p. 266–294, https://doi.org/10.1016/j.earscirev.2017.07.016.

Geng, J.Z., Li, H.K., Zhang, J., Zhou, H.Y., and Li, H.M., 2011, Zircon Hf isotope analysis by means of LA-MC-ICP-MS: Dizhi Tongbao, v. 30, no. 10, p. 1508–1513 [in Chinese with English abstract].

Grimes, C.B., Wooden, J.L., Cheadle, M.J., and John, B.E., 2015, "Fingerprinting" tectono-magmatic provenance using trace elements in igneous zircon: Contributions to Mineralogy and Petrology, v. 170, no. 5–6, p. 46, https://doi.org/10.1007/s00410-015-1199-3.

Halpin, J.A., Tran, H.T., Lai, C.K., Meffre, S., Crawford, A.J., and Zaw, K., 2016, U–Pb zircon geochronology and geochemistry from NE Vietnam: A 'tectonically disputed' territory between the Indochina and South China blocks: Gondwana Research, v. 34, p. 254–273, https://doi.org/10.1016/j.gr.2015.04.005.

Harris, N.B.W., Pearce, J.A., and Tindle, A.G., 1986, Geochemical characteristics of collision zone magmatism, *in* Coward, M.P., and Ries, A.C., eds., Collision Tectonics: Geological Society, London, Special Publication 19, p. 67–81, https://doi.org/10.1144/GSL.SP.1986.019.01.04.

He, W., Yang, L., Lu, Y., Jeon, H., Xie, S., and Gao, X., 2018, Zircon U-Pb dating, geochemistry and Sr-Nd-Hf-O isotopes for the Baimaxueshan granodiorites and mafic microgranulars enclaves in the Sanjiang Orogen: Evidence for westward subduction of Paleo-Tethys: Gondwana Research, v. 62, p. 112–126, https://doi.org/10.1016/j.gr.2018.03.011.

Hennig, D., Lehmann, B., Frei, D., Belyatsky, B., Zhao, X.F., Cabral, A.R., Zeng, P.S., Zhou, M.F., and Schmidt, K., 2009, Early Permian seafloor to continental arc magmatism in the eastern Paleo-Tethys: U-Pb age and Nd-Sr isotope data from the southern Lancangjiang zone, Yunnan, China: Lithos, v. 113, no. 3–4, p. 408–422, https://doi.org/10.1016/j.lithos.2009.04.031.

Hofmann, A.W., and White, W.M., 1983, Ba, Rb, and Cs in the Earth's Mantle: Zeitschrift Naturforschung Teil A, v. 38, p. 256–266, https://doi.org/10.1515/zna-1983-0225.

Hoskin, P.W.O., and Ireland, T.R., 2000, Rare earth element chemistry of zircon and its use as a provenance indicator: Geology, v. 28, no. 7, p. 627–630, https://doi.org/10.1130/0091-7613(2000)28<627:REECOZ>2.0.CO;2.

Hoskin, P.W.O., and Schaltegger, U., 2003, The composition of zircon and igneous and metamorphic petrogenesis: Reviews in Mineralogy and Geochemistry, v. 53, no. 1, p. 27–62, https://doi.org/10.2113/0530027.

Hou, Y.L., Zhong, Y.T., Xu, Y.G., and He, B., 2017, The provenance of late Permian karstic bauxite deposits in SW China, constrained by the geochemistry of interbedded clastic rocks, and U-Pb-Hf-O isotopes of detrital zircons: Lithos, v. 278–281, p. 240–254, https://doi.org/10.1016/j.lithos.2017.01.013.

Hu, J., Li, Q., Li, J., Huang, J., and Ge, D., 2015a, Geochemical characteristics and depositional environment of the Middle Permian mudstones from central Qiangtang Basin, northern Tibet: Geological Journal, v. 51, no. 4, p. 560–571, https://doi.org/10.1002/gj.2653.

Hu, L., Cawood, P., Du, Y., Xu, Y., Xu, W.C., and Huang, H., 2015b, Detrital records for Upper Permian–Lower Triassic succession in the Shiwandashan Basin, South China and implication for Permo-Triassic (Indosinian) orogeny: Journal of Asian Earth Sciences, v. 98, p. 152–166, https://doi.org/10.1016/j.jseaes.2014.11.007.

Hu, L.S., Du, Y.S., Yang, J.H., Huang, H., Huang, H.W., and Huang, Z.Q., 2012, Geochemistry and Tectonic Significance of Middle Triassic Volcanic Rocks in Nalong, Guangxi Area: Geological Review (Dizhi Lunping), v. 58, no. 3, p. 481–494 [in Chinese with English abstract].

Hu, R., Fu, S., Huang, Y., Zhou, M.F., Fu, S., Zhao, C., Wang, Y., Bi, X., and Xiao, J., 2017, The giant South China Mesozoic low-temperature metallogenic domain: Reviews and a new geodynamic model: Journal of Asian Earth Sciences, v. 137, p. 9–34, https://doi.org/10.1016/j.jseaes.2016.10.016.

Hu, Z., Liu, Y., Gao, S., Hu, S., Dietiker, R., and Günther, D., 2008, A local aerosol extraction strategy for the determination of the aerosol composition in laser ablation inductively coupled plasma mass spectrometry: Journal of Analytical Atomic Spectrometry, v. 23, p. 1192–1203, https://doi.org/10.1039/b803934h.

Huang, H.Q., Li, X.H., Li, W.X., and Li, Z.X., 2011, Formation of high $\delta^{18}O$ fayalite-bearing A-type granite by high-temperature melting of granulitic metasedimentary rocks, southern China: Geology, v. 39, no. 10, p. 903–906, https://doi.org/10.1130/G32080.1.

Huang, W.M., Liu, X.J., Li, Z.L., Wei, Y.L., Guo, J.L., Han, Y.Y., and Zhao, B., 2022, Tectonic evolution of the Paleo-Tethys Ocean in southwest Guangxi: evidence from granites in Pingxiang area, SW China: Journal of Guilin University of Technology, v. 42, no. 2, p. 281–294 [in Chinese with English abstract].

Jiao, S., Li, X.H., Huang, H.Q., and Deng, X., 2015, Metasedimentary melting in the formation of charnockite: Petrological and zircon U-Pb-Hf-O isotope evidence from the Darongshan S-type granitic complex in southern China: Lithos, v. 239, p. 217–233, https://doi.org/10.1016/j.lithos.2015.10.004.

Karsli, O., Aydin, F., Uysal, I., Dokuz, A., Kumral, M., Kandemir, R., Budakoglu, M., and Ketenci, M., 2018, Latest Cretaceous "A_2-type" granites in the Sakarya Zone, NE Turkey: Partial melting of mafic lower crust in response to roll-back of Neo-Tethyan oceanic lithosphere: Lithos, v. 302–303, p. 312–328, https://doi.org/10.1016/j.lithos.2017.12.025.

Ke, X., Zhang, Z., Yang, J., Yao, H., Zhu, L., and He, W., 2018, Radiolarian and Detrital Zircon in the Upper Carboniferous to Permian Bancheng Formation, Qinfang Basin, and the Geological Significance: Journal of Earth Science, v. 29, p. 594–606, https://doi.org/10.1007/s12583-017-0938-y.

Kemp, A.I.S., Wormald, R.J., Whitehouse, M.J., and Price, R.C., 2005, Hf isotopes in zircon reveal contrasting sources and crystallization histories for alkaline to peralkaline granites of Temora, southeastern Australia: Geology, v. 33, no. 10, p. 797–800, https://doi.org/10.1130/G21706.1.

King, P.L., Chappell, B.W., Allen, C.M., and White, A.J.R., 2001, Are A-type granites the high-temperature felsic granites? Evidence from fractionated granites of the Wangrah Suite: Australian Journal of Earth Sciences, v. 48, no. 4, p. 501–514, https://doi.org/10.1046/j.1440-0952.2001.00881.x.

Lai, K., Meffre, S., Crawford, A., Zaw, K., Xue, C., and Halpin, J., 2014, The Western Ailaoshan Volcanic Belts and their SE Asia connection: A new tectonic model for the Eastern Indochina Block: Gondwana Research, v. 26, p. 52–74, https://doi.org/10.1016/j.gr.2013.03.003.

Landenberger, B., and Collins, W.J., 1996, Derivation of A-type Granites from a Dehydrated Charnockitic Lower Crust: Evidence from the Chaelundi Complex, Eastern Australia: Journal of Petrology, v. 37, no. 1, p. 145–170, https://doi.org/10.1093/petrology/37.1.145.

Lepvrier, C., Maluski, H., Tich, V., Leyreloup, A., Thi, P., and Vuong, N., 2004, The Early Triassic Indosinian orogeny in Vietnam (Truong Son Belt and Kontum Massif); implications for the geodynamic evolution of Indochina: Tectonophysics, v. 393, no. 1–4, p. 87–118, https://doi.org/10.1016/j.tecto.2004.07.030.

Li, G.Z., 2014, Petrological and geochemical evidence for early Permian intra-oceanic subduction in the Palaeo-Tethys Ocean, Sanjiang area, SW China [Ph.D. thesis]: Beijing, China University of Geosciences [in Chinese with English abstract], 74 p.

Li, J., Zhao, G., Johnston, S.T., Dong, S., Zhang, Y., Xin, Y., Wang, W., Sun, H., and Yu, Y., 2017, Permo-Triassic structural evolution of the Shiwandashan and Youjiang structural belts, South China: Journal of Structural Geology, v. 100, p. 24–44, https://doi.org/10.1016/j.jsg.2017.05.004.

Li, W., Ma, C., Liu, Y., and Robinson, P.T., 2012a, Discovery of the Indosinian aluminum A-type granite in Zhejiang Province and its geological significance: Science China Earth Sciences, v. 55, no. 1, p. 13–25, https://doi.org/10.1007/s11430-011-4351-6.

Li, X.H., Li, Z.X., Li, W.X., and Wang, Y., 2006, Initiation of the Indosinian Orogeny in South China: Evidence for a Permian Magmatic Arc on Hainan Island: The Journal of Geology, v. 114, no. 3, p. 341–353, https://doi.org/10.1086/501222.

Li, X.H., Li, W.X., Li, Z.X., Lo, C.H., Wang, J., Ye, M.F., and Yang, Y.H., 2009, Amalgamation between the Yangtze and Cathaysia Blocks in South China: Constraints from SHRIMP U-Pb zircon ages, geochemistry and Nd-Hf isotopes of the Shuangxiwu volcanic rocks: Precambrian Research, v. 174, no. 1–2, p. 117–128, https://doi.org/10.1016/j.precamres.2009.07.004.

Li, X.H., Li, Z.X., He, B., Li, W.X., Li, Q.L., Gao, Y., and Wang, X.C., 2012b, The Early Permian active continental margin and crustal growth of the Cathaysia Block: In situ U-Pb, Lu-Hf and O isotope analyses of detrital zircons: Chemical Geology, v. 328, no. 1, p. 195–207, https://doi.org/10.1016/j.chemgeo.2011.10.027.

Li, Y.J., Wei, J.H., Santosh, M., Tan, J., Fu, L.B., and Zhao, S.Q., 2016, Geochronology and petrogenesis of Middle Permian

S-type granitold in southeastern Guangxi Province, South China: Implications for closure of the eastern Paleo-Tethys: Tectonophysics, v. 682, p. 1–16, https://doi.org/10.1016/j.tecto.2016.05.048.

Li, Z.L., Liu, X.J., Xiao, W.J., Bao, H.Y., Shi, Y., Liu, L., Liao, S., and Qin, X.Z., 2019, Geochronology, geochemistry and Hf isotopes of volcanic rocks in Pingxing area, southwest Guangxi: Implications for the latest stage of Paleo-Tethyan Ocean northward subduction: Journal of Geometry, v. 25, no. 5, p. 932–946 [in Chinese with English abstract].

Li, Z.X., and Li, X.H., 2007, Formation of the 1300-km-wide intracontinental orogen and postorogenic magmatic province in Mesozoic South China: A flat-slab subduction model: Geology, v. 35, no. 2, p. 179–182, https://doi.org/10.1130/G23193A.1.

Liu, C., Deng, J.F., Liu, J.L., and Shi, Y.L., 2011, Characteristics of volcanic rocks from Late Permian to Early Triassic in Ailaoshan tectono-magmatic belt and implications for tectonic settings: Acta Petrologica Sinica (Yanshi Xuebao), v. 27, p. 3590–3602 [in Chinese with English abstract].

Liu, H., Wang, Y., Cawood, P.A., Fan, W., Cai, Y., and Xing, X., 2015, Record of Tethyan ocean closure and Indosinian collision along the Ailaoshan suture zone (SW China): Gondwana Research, v. 27, no. 3, p. 1292–1306, https://doi.org/10.1016/j.gr.2013.12.013.

Liu, H., Wang, Y., Cawood, P.A., and Guo, X., 2017, Episodic slab rollback and back-arc extension in the Yunnan-Burma region: Insights from Cretaceous Nb-enriched and oceanic-island basalt–like mafic rocks: Geological Society of America Bulletin, v. 129, no. 5–6, p. 698–714, https://doi.org/10.1130/B31604.1.

Liu, H., Peng, T., and Guo, X., 2018, Geochronological and geochemical constraints on the coexistent N-MORB and SSZ type ophiolites in Babu area (SW China) and tectonic implications: Journal of the Geological Society of London, v. 175, no. 4, p. 667–678, https://doi.org/10.1144/jgs2017-121.

Liu, J., Tran, M.D., Tang, Y., Quang, L., Tran, H., Wu, W., Chen, J.F., Zhang, Z., and Zhao, Z., 2012, Permo-Triassic granitoids in the northern part of the Truong Son belt, NW Vietnam: Geochronology, Geochemistry and tectonic implications: Gondwana Research, v. 22, p. 628–644, https://doi.org/10.1016/j.gr.2011.10.011.

Liu, X.J., Zhang, Z.G., Xu, J.F., Xiao, W.J., Shi, Y., Gong, X.H., Tan, Z.J., and Li, R., 2020, The youngest Permian Ocean in Central Asian Orogenic Belt: Evidence from Geochronology and Geochemistry of Bingdaban Ophiolitic Mélange in Central Tianshan, northwestern China: Geological Journal, v. 55, no. 3, p. 2062–2079, https://doi.org/10.1002/gj.3698.

Liu, Y., Gao, S., Hu, Z., Gao, C., Zong, K., and Wang, D., 2010a, Continental and Oceanic Crust Recycling-induced Melt—Peridotite Interactions in the Trans-North China Orogen: U-Pb Dating, Hf Isotopes and Trace Elements in Zircons from Mantle Xenoliths: Journal of Petrology, v. 51, no. 1–2, p. 537–571, https://doi.org/10.1093/petrology/egp082.

Liu, Y., Hu, Z., Zong, K., Gao, C., Gao, S., Xu, J., and Chen, H., 2010b, Reappraisement and refinement of zircon U-Pb isotope and trace element analyses by LA-ICP-MS: Chinese Science Bulletin, v. 55, no. 15, p. 1535–1546, https://doi.org/10.1007/s11434-010-3052-4.

Ludwig, K., 2003, User's Manual for Isoplot 3.00: A Geochronological Toolkit for Microsoft Excel: Berkeley Geochronology Center Special Publication 4, 74 p.

Maniar, P.D., and Piccoli, P.M., 1989, Tectonic discrimination of granitoids: Geological Society of America Bulletin, v. 101, no. 5, p. 635–643, https://doi.org/10.1130/0016-7606(1989)101<0635:TDOG>2.3.CO;2.

Metcalfe, I., 2011, Palaeozoic–Mesozoic history of SE Asia, *in* Hall, R., et al., eds., The SE Asian Gateway: History and Tectonics of the Australia–Asia Collision: Geological Society, London, Special Publication 355, p. 7–35, https://doi.org/10.1144/SP355.2.

Mushkin, A., Navon, O., Halicz, L., Hartmann, G., and Stein, M., 2003, The Petrogenesis of A-type Magmas from the Amram Massif, Southern Israel: Journal of Petrology, v. 44, no. 5, p. 815–832, https://doi.org/10.1093/petrology/44.5.815.

Nakakuki, T., and Mura, E., 2013, Dynamics of slab rollback and induced back-arc basin formation: Earth and Planetary Science Letters: A Letter Journal Devoted to the Development in Time of the Earth and Planetary System: Earth and Planetary Science Letters, v. 361, p. 287–297, https://doi.org/10.1016/j.epsl.2012.10.031.

Niu, Y., 2014, Geological understanding of plate tectonics: Basic concepts, illustrations, examples and new perspectives: Global Tectonics and Metallogeny, v. 10, p. 23–46, https://doi.org/10.1127/gtm/2014/0009.

Patiño Douce, A., 1999, What do experiments tell us about the relative contributions of crust and mantle to the origin of granitic magmas? *in* Castro, A., eds., Understanding Granites: Integrating New and Classical Techniques: Geological Society, London, Special Publication 168, p. 55–75, https://doi.org/10.41144/GSI.SP.1999.168.01.05.

Patiño Douce, A.E., 1997, Generation of metaluminous A-type granites by low-pressure melting of calc-alkaline granitoids: Geology, v. 25, no. 8, p. 743–746, https://doi.org/10.1130/0091-7613(1997)025<0743:GOMATG>2.3.CO;2.

Pearce, J.A., and Gale, G.H., 1977, Identification of ore-deposition environment from trace-element geochemistry of associated igneous host rocks, *in* Gass, I.G., ed., Volcanic Processes in Ore Genesis: Geological Society, London, Special Publication 7, p. 14–24, https://doi.org/10.1144/GSL.SP.1977.007.01.03.

Peng, T., Wang, Y., Zhao, G., Fan, W., and Peng, B., 2008, Arc-like volcanic rocks from the southern Lancangjiang zone, SW China: Geochronological and geochemical constraints on their petrogenesis and tectonic implications: Lithos, v. 102, no. 1–2, p. 358–373, https://doi.org/10.1016/j.lithos.2007.08.012.

Peng, T., Wilde, S.A., Wang, Y., Fan, W., and Peng, B., 2013, Mid-Triassic felsic igneous rocks from the southern Lancangjiang Zone, SW China: Petrogenesis and implications for the evolution of Paleo-Tethys: Lithos, v. 168–169, p. 15–32, https://doi.org/10.1016/j.lithos.2013.01.015.

Peng, T.P., 2006, The Triassic post-collisional magmatism for the southern Lancangjiang tectonic zone, southwestern China: Petrogenesis and its tectonic implications [Ph.D. thesis]: Guangzhou, School of the Chinese Academy of Sciences [in Chinese with English abstract], 108 p.

Pham, T.T., Shellnutt, J.G., Tran, T.A., and Lee, H.Y., 2020, Petrogenesis of Eocene to early Oligocene granitic rocks in Phan Si Pan uplift area, northwestern Vietnam: Geochemical implications for the Cenozoic crustal evolution of the South China Block: Lithos, v. 372–373, https://doi.org/10.1016/j.lithos.2020.105640.

Qi, C.S., Deng, X.G., Li, W.X., Li, X.H., Yang, Y.H., and Xie, L.W., 2007, Origin of the Darongshan-Shiwangdashan S-type granitoid belt from southeastern Guangxi: geochemical and Sr-Nd-Hf isotopic constraints: Acta Petrologica Sinica (Yanshi Xuebao), no. 2, p. 403–412 [in Chinese with English abstract].

Qin, H.F., Huang, X.Q., Jiang, J., Tan, B., Pang, J.G., and Xie, Z.G., 2018, Genesis of Indosinian granites in Maoershan, northern Guangxi: Evidence from petrology, geochemistry, zircon U-Pb ages and Hf isotope: Journal of Guilin University of Technology, v. 38, no. 4, p. 597–613 [in Chinese with English abstract].

Qin, X.F., Wang, Z.Q., Zhang, Y.L., Pang, L.Z., Hu, G.A., and Zhou, F.S., 2011, Geochronology and geochemistry of Early Mesozoic acid volcanic rocks from Southwest Guangxi: Constraints on tectonic evolution of the southwestern segment of QinzhouHangzhou joint belt: Acta Petrologica Sinica (Yanshi Xuebao), v. 27, no. 3, p. 794–808 [in Chinese with English abstract].

Qin, X.F., Wang, Z.Q., Zhang, Y.L., Pan, L.Z., Hu, G.A., and Zhou, F.S., 2012, Geochemistry of Permian Mafic Igneous Rocks from the Napo-Qinzhou Tectonic Belt in Southwest Guangxi, Southwest China: Implications for Arc-Back Arc Basin Magmatic Evolution: Acta Geologica Sinica, v. 86, no. 5, p. 1182–1199, https://doi.org/10.1111/j.1755-6724.2012.00740.x.

Qin, X.F, Wang, Z.Q., Cao, J., Feng, Z.H., Hu, G.A., and Peng, L.Z., 2013, Petrogenesis of Early Indosinian Granites from the Southwestern Segment of Qinfang Tectonic Belt, Southern Guangxi: Constraints from Zircon U-Pb Chronology and Geochemistry: Journal of Jilin University (Earth Science Edition), v. 43, no. 5, p. 1471–1488 [in Chinese with English abstract].

Qiu, L., Yan, D.P., Yang, W.X., Wang, J., Tang, X., and Ariser, S., 2017, Early to Middle Triassic sedimentary records in the Youjiang Basin, South China: Implications for Indosinian orogenesis: Journal of Asian Earth Sciences, v. 141, p. 125–139, https://doi.org/10.1016/j.jseaes.2016.09.020.

Rudnick, R.L., and Fountain, D.M., 1995, Nature and composition of the continental crust: A lower crustal perspective: Reviews of Geophysics, v. 33, no. 3, p. 267–309, https://doi.org/10.1029/95RG01302.

Rudnick, R.L., and Gao, S., 2003, 3.01-Composition of the Continental Crust, *in* Holland, H.D., and Turekian, K.K., eds., Treatise on Geochemistry: Elsevier, v. 3, p. 1–64, https://doi.org/10.1016/B0-08-043751-6/03016-4.

Schandl, E.S., and Gorton, M.P., 2002, Application of high field strength elements to discriminate tectonic settings in VMS environments: Economic Geology, v. 97, no. 3, p. 629–642, https://doi.org/10.2113/gsecongeo.97.3.629.

Shen, W.Z., Zhu, J.C., Liu, C.S., Xu, S.J., and Ling, H.F., 1993, Sm-Nd Isotopic Study of Basement Metamorphic Rocks in South China and Its Constraint on Material Sources of Granitoids: Acta Petrologica Sinica (Yanshi Xuebao), v. 9, no. 2, p. 115–124 [in Chinese with English abstract].

Song, B., Yan, Q.R., Xiang, Z.J., Chen, H.M., and Li, J.L., 2014, Petrography and geochemistry of clastic rocks and their constraints on the tectonic setting of the Middle Triassic Pingxiang basin, Southern Part of Guangxi: Dizhi Tongbao, v. 33, no. 12, p. 2032–2050 [in Chinese with English abstract].

Sun, S.S., and McDonough, W.F., 1989, Chemical and isotopic systematics of oceanic basalts: Implications for mantle composition and processes, *in* Saunders, A.D., and Norry, M.J., eds., Magmatism in the Ocean Basins: Geological Society, London, Special Publication 42, p. 313–345, https://doi.org/10.1144/GSL.SP.1989.042.01.19.

Sun, X.M., and Jian, P., 2004, The Wilson cycle of the Jinshajiang PaleoTethys ocean, in Western Yunnan and Western Sichuan provinces: Geological Review (Dizhi Lunping), v. 50, no. 4, p. 343–350, https://doi.org/10.16509/j.georeview.2004.04.002.

Turner, S.P., Foden, J.D., and Morrison, R.S., 1992, Derivation of some A-type magmas by fractionation of basaltic magma: An example from the Padthaway Ridge, South Australia: Lithos, v. 28, no. 2, p. 151–179, https://doi.org/10.1016/0024-4937(92)90029-X.

Uyeda, S., and Kanamori, H., 1979, Back-arc opening and the mode of subduction: Journal of Geophysical Research, v. 84, no. B3, p. 1049–1061, https://doi.org/10.1029/JB084iB03p01049.

Wang, B.D., Wang, L.D., Wang, D.B., Yi, F.G., He, J., Peng, Z.M., and Yan, G.C., 2018a, Tectonic evolution of the Changning-Menglian proto-Paleo Tethys ocean in the Sanjiang area, southwestern China: Earth Science, v. 43, no. 8, p. 2527–2550 [in Chinese with English abstract].

Wang, Q., Yang, L., Xu, X., Santosh, M., Wang, Y., Wang, T., Chen, F., Wang, R., Gao, L., Liu, X., Yang, S., Zeng, Y., Chen, J., Zhang, Q., and Deng, J., 2020, Multi-stage tectonics and metallogeny associated with Phanerozoic evolution of the South China Block: A holistic perspective from the Youjiang Basin: Earth-Science Reviews, v. 211, https://doi.org/10.1016/j.earscirev.2020.103405.

Wang, Y., and Deng, J.F., 2003, The geodynamic significance of petrochemical features of Triassic strongly peraluminous igneous rocks in the southern part of Guangxi Province: Geology Geochemistry, v. 31, no. 4, p. 35–42 [in Chinese with English abstract].

Wang, Y., Qian, X., Cawood, P.A., Liu, H., Feng, Q., Zhao, G., Zhang, Y., He, H., and Zhang, P., 2018b, Closure of the East Paleotethyan Ocean and amalgamation of the Eastern Cimmerian and Southeast Asia continental fragments: Earth-Science Reviews, v. 186, p. 195–230, https://doi.org/10.1016/j.earscirev.2017.09.013.

Wang, Y., Wang, Q., Deng, J., Xue, S., Li, C., and Ripley, E.M., 2021, Late Permian–Early Triassic mafic dikes in the southwestern margin of the South China block: Evidence for Paleo-Pacific subduction: Lithos, v. 384–385, https://doi.org/10.1016/j.lithos.2021.105994.

Wang, Z., Xu, D.R., Wu, C.J., Fu, W.W., Wang, L., and Wu, J.J., 2013, Discovery of the Late Paleozoic ocean island basalts (OIB) in Hainan Island and their geodynamic implications: Acta Petrologica Sinica (Yanshi Xuebao), v. 29, p. 875–886 [in Chinese with English abstract].

Wei, C.X., Lu, G., Yang, F., Li, W., Zhong, F.Y., Jin, J.J., Pan, Y.W., Liang, L.J., Bai, X., Pang, T.W., and Wang, Y.F., 2020, Zircon U-Pb-Hf isotopic composition constraints for its Source Characteristics of volcanic rocks in the Liudong area: Geology in China, p. 1–18 [in Chinese with English abstract].

Wei, Q.R., and Shen, S.Y., 1997, Arc volcanic rocks of late Permian (P_2) in Taizhong-Lixianjiang zone, Ailaoshan area: Jmineral Petrol, v. 17, p. 8–16 [in Chinese with English abstract].

Wei, Y., Zhao, Z., Niu, Y., Zhu, D.C., Liu, D., Wang, Q., Hou, Z., Mo, X., and Wei, J., 2017, Geochronology and geochemistry of the Early Jurassic Yeba Formation volcanic rocks in southern Tibet: Initiation of back-arc rifting and crustal accretion in the southern Lhasa Terrane: Lithos, v. 278–281, p. 477–490, https://doi.org/10.1016/j.lithos.2017.02.013.

Whalen, J.B., Currie, K.L., and Chappell, B.W., 1987, A-type granites: geochemical characteristics, discrimination and petrogenesis: Contributions to Mineralogy and Petrology, v. 95, no. 4, p. 407–419, https://doi.org/10.1007/BF00402202.

Wilson, M., 1989, Igneous Petrogenesis: A Global Tectonic Approach: Mineralogical Magazine, v. 53, no. 372, p. 514–515, https://doi.org/10.1180/minmag.1989.053.372.15.

Wu, F.Y., Yang, Y.H., Xie, L.W., Yang, J.H., and Xu, P., 2006, Hf isotopic compositions of the standard zircons and baddeleyites used in U–Pb geochronology: Chemical Geology, v. 234, no. 1–2, p. 105–126, https://doi.org/10.1016/j.chemgeo.2006.05.003.

Wu, G., Zhong, D., Zhang, Q., and Ji, J.Q., 1999, Babu-Phu Ngu Ophiolites: A Geological Record of Paleotethyan Ocean Bordering China and Vietnam: Gondwana Research, v. 2, no. 4, p. 554–557, https://doi.org/10.1016/S1342-937X(05)70193-3.

Wu, G.Y., Wu, H.R., Zhong, D.L., Kuang, G.D., and Ji, J.Q., 2000, Volcanic rocks of paleotethyan oceanic island and island-arc bordering Yunnan and Guangxi, China: Modern Geology, v. 14, no. 4, p. 393–400 [in Chinese with English abstract].

Wu, G.Y., Ji, J.Q., He, S.D., and Zhong, D.L., 2002, Early Permian magmatic arc in Pingxiang, Guangxi and its tectonic implications: Mineralogy and Petrology, v. 22, no. 3, p. 61–65, https://doi.org/10.19719/j.cnki.1001-6872.2002.03.014 [in Chinese with English abstract].

Wu, H., Li, C., Chen, J., and Xie, C., 2015, Late Triassic tectonic framework and evolution of Central Qiangtang, Tibet, SW China: Lithosphere, v. 8, no. 2, p. 141–149, https://doi.org/10.1130/L468.1.

Wu, H., Zhang, Y., Wang, F.F., Song, W.Y., Bai, F.L., Xue, B.Y., and Bi, S.P., 2022, Petrogenesis of Cretaceous volcanic rocks from islands off Fujian Province, East China Sea, and implications for episodic slab rollback of the paleo-Pacific plate: Gondwana Research, v. 103, p. 243–259, https://doi.org/10.1016/j.gr.2021.10.006.

Xia, Y., and Xu, X., 2020, The epilogue of Paleo-Tethyan tectonics in the South China Block: Insights from the Triassic aluminous A-type granitic and bimodal magmatism: Journal of Asian Earth Sciences, v. 190, https://doi.org/10.1016/j.jseaes.2019.104129.

Xia, Y., Xu, X., Niu, Y., and Liu, L., 2018, Neoproterozoic amalgamation between Yangtze and Cathaysia blocks: The magmatism in various tectonic settings and continent-arc-continent collision: Precambrian Research, v. 309, p. 56–87, https://doi.org/10.1016/j.precamres.2017.02.020.

Xiang, Z.J., Yan, Q.R., Xia, L., and Xia, W.J., 2021, The tectonic setting of the Early-Middle Triassic volcanic-sedimentary succession in Funing-Napo area, the south margin of Nanpanjiang Basin, South China: Dizhi Tongbao, v. 40, no. 1, p. 138–151 [in Chinese with English abstract].

Xin, D., 2018, The main suture of Paleo-Tethys and its tectonic evolution in middle Sanjiang Orogenic belt [Ph.D. thesis]: Beijing, Chinese Academy of Geological Sciences [in Chinese with English abstract], 160 p.

Xin, D., Yang, T.N., Liang, M.J., Xue, C.D., Han, X., Liao, C., and Tang, J., 2018, Syn-subduction crustal shortening produced a magmatic flare-up in middle Sanjiang orogenic belt, southeastern Tibet Plateau: Evidence from geochronology, geochemistry, and structural geology: Gondwana Research, v. 62, p. 93–111, https://doi.org/10.1016/j.gr.2018.03.009.

Xu, D.R., Xia, B., Li, P.C., Chen, G.H., Ma, C., and Zhang, Y.Q., 2007, Protolith natures and U-Pb sensitive high mass-resolution ion microprobe (SHRIMP) zircon ages of the metabasites in Hainan Island, South China: Implications for geodynamic evolution since the late Precambrian: The Island Arc, v. 16, no. 4, p. 575–597, https://doi.org/10.1111/j.1440-1738.2007.00584.x.

Xu, J., Xia, X., Lai, K., Long, X., and Huang, C., 2019, When Did the Paleotethys Ailaoshan Ocean Close: New Insights from Detrital Zircon U-Pb age and Hf Isotopes: Tectonics, v. 38, p. 1798–1823, https://doi.org/10.1029/2018TC005291.

Xu, J., Xia, X., Cai, K., Lai, K., Liu, X., Yang, Q., Zhou, M.L., Ma, P.F., and Zhang, L., 2020, Remnants of a Middle Triassic island arc on western margin of South China Block: Evidence for bipolar subduction of the Paleotethyan Ailaoshan Ocean: Lithos, v. 360–361, https://doi.org/10.1016/j.lithos.2020.105447.

Xu, W.C., Luo, B.J., Xu, Y.J., Wang, L., and Chen, Q., 2018, Geochronology, geochemistry, and petrogenesis of late Permian to early Triassic mafic rocks from Darongshan, South China: Implications for ultrahigh-temperature metamorphism and S-type granite generation: Lithos, v. 308–309, p. 168–180, https://doi.org/10.1016/j.lithos.2018.03.004.

Yadav, B.S., Ahmad, T., Kaulina, T., Bayanova, T., and Bhutani, R., 2020, Origin of post-collisional A-type granites in the Mahakoshal Supracrustal Belt, Central Indian Tectonic Zone, India: Zircon U-Pb ages and geochemical evidences: Journal of Asian Earth Sciences, v. 191, https://doi.org/10.1016/j.jseaes.2020.104247.

Yang, J.H., Wu, F.Y., Chung, S.L., Wilde, S.A., and Chu, M.F., 2006, A hybrid origin for the Qianshan A-type granite, northeast China: Geochemical and Sr-Nd–Hf isotopic evidence: Lithos, v. 89, no. 1–2, p. 89–106, https://doi.org/10.1016/j.lithos.2005.10.002.

Yang, L., Wang, Q., Wang, Y., and Li, G., 2018, Proto- to Paleo-Tethyan evolution of the eastern margin of Simao block: Gondwana Research, v. 62, p. 61–74, https://doi.org/10.1016/j.gr.2018.02.012.

Yang, L., Wang, C., Du, B., Chen, Q., He, Z., and Zhu, J., 2020, Sequence and petrogenesis of the volcanic rocks from the middle Sanjiang Tethys Orogen, SW China: Implications for the Sanjiang Paleo-Tethyan evolution: Geological Journal, v. 55, no. 9, p. 6235–6254, https://doi.org/10.1002/gj.3806.

Yang, T.N., Hou, Z.Q., Wang, Y., Zhang, H.R., and Wang, Z.L., 2012, Late Paleozoic to Early Mesozoic tectonic evolution of northeast Tibet: Evidence from the Triassic composite western Jinsha-Garzê-Litang suture: Tectonics, v. 31, no. 4, https://doi.org/10.1029/2011TC003044.

Yang, T.N., Liang, M.J., Fan, J.W., Shi, P.L., Zhang, H.R., and Hou, Z.H., 2014, Paleogene sedimentation, volcanism, and deformation in eastern Tibet: Evidence from structures, geochemistry, and zircon U-Pb dating in the Jianchuan Basin, SW China: Gondwana Research, v. 26, no. 2, p. 521–535, https://doi.org/10.1016/j.gr.2013.07.014.

Yao, J., Cawood, P.A., Shu, L., and Zhao, G., 2019, Jiangnan Orogen, South China: A ~970–820 Ma Rodinia margin accretionary belt: Earth-Science Reviews, v. 196, 102872, https://doi.org/10.1016/j.earscirev.2019.05.016.

Yuan, H.L., Gao, S., Dai, M.N., Zong, C.L., Günther, D., Fontaine, G.H., Liu, X.M., and Diwu, C., 2008, Simultaneous determinations of U-Pb age, Hf isotopes and trace element

compositions of zircon by excimer laser-ablation quadrupole and multiple-collector ICP-MS: Chemical Geology, v. 247, no. 1–2, p. 100–118, https://doi.org/10.1016/j.chemgeo.2007.10.003.

Zhang, H., Yu, Y.S., Wang, X.M., He, H., Xiao, P., and Wang, F.M., 2017, Zircon U-Pb geochronology and geological significance of volcanic rocks from the western margin of Lanping Basin, Sanjiang Orogenic Belt, China: Acta Mineralogica Sinica, v. 37, no. 5, p. 596–607, https://doi.org/10.16461/j.cnki.1000-4734.2017.05.010.

Zhang, H., Yang, T., Hou, Z., and Wang, Y., 2020, Magmatic expression of tectonic transition from oceanic subduction to continental collision: Insights from the Middle Triassic rhyolites of the North Qiangtang Block: Gondwana Research, v. 87, p. 67–82, https://doi.org/10.1016/j.gr.2020.05.012.

Zhang, R., Lo, C.H., Li, X.H., Chung, S.L., Anh, T., and Tri, T., 2014, U-Pb dating and tectonic implication of ophiolite and metabasite from the Song Ma suture zone, northern Vietnam: American Journal of Science, v. 314, p. 649–678, https://doi.org/10.2475/02.2014.07.

Zhang, X., Yuan, L., Xue, F., Yan, X., and Mao, Q., 2015, Early Permian A-type granites from central Inner Mongolia, North China: Magmatic tracer of post-collisional tectonics and oceanic crustal recycling: Gondwana Research, v. 28, no. 1, p. 311–327, https://doi.org/10.1016/j.gr.2014.02.011.

Zhao, G., 2015, Jiangnan Orogen in South China: Developing from divergent double subduction: Gondwana Research, v. 27, no. 3, p. 1173–1180, https://doi.org/10.1016/j.gr.2014.09.004.

Zhao, T., Cawood, P.A., Wang, K., Zi, J.W., Feng, Q., Nguyen, Q.M., and Tran, D.M., 2019, Neoarchean and Paleoproterozoic K-rich granites in the Phan Si Pan Complex, north Vietnam: Constraints on the early crustal evolution of the Yangtze Block: Precambrian Research, v. 332, https://doi.org/10.1016/j.precamres.2019.105395.

Zhao, X.F., Zhou, M.F., Li, J.W., and Wu, F.Y., 2008, Association of Neoproterozoic A- and I-type granites in South China: Implications for generation of A-type granites in a subduction-related environment: Chemical Geology, v. 257, no. 1–2, p. 1–15, https://doi.org/10.1016/j.chemgeo.2008.07.018.

Zi, J.W., Cawood, P., Fan, W.M., Tohver, E., Wang, Y., and McCuaig, T., 2012a, Generation of Early Indosinian enriched mantle-derived granitoid pluton in the Sanjiang Orogen (SW China) in response to closure of the Paleo-Tethys: Lithos, v. 140–141, p. 166–182, https://doi.org/10.1016/j.lithos.2012.02.006.

Zi, J.W., Cawood, P., Fan, W.M., Wang, Y., and Tohver, E., 2012b, Contrasting rift and subduction-related plagiogranites in the Jinshajiang ophiolitic mélange, southwest China, and implications for the Paleo-Tethys: Tectonics, v. 31, TC2012, https://doi.org/10.1029/2011TC002937.